Dominant recombination path in low-bandgap kesterite CZTSe(S) solar cells from red light induced metastability EP

Mbafan S. Lyam,[1,2,a] Torsten Hölscher,[1] Matthias Maiberg,[1] Antonio Cabas-Vidani,[3]
Alejandro Hernandez-Martinez,[4] Hitoshi Tampo,[5] and Roland Scheer[1]

AFFILIATIONS

[1]Photovoltaics Group, Martin Luther University Halle-Wittenberg, 06120 Halle (Saale), Germany
[2]Department of Physics, Benue State University, Makurdi PMB 102119, Nigeria
[3]Swiss Federal Laboratories for Materials Science and Technology Empa, Ueberlandstrasse 129, 8600 Dübendorf, Switzerland
[4]Catalonia Institute for Energy Research (IREC), 08930 Sant Adria de Besos, Barcelona, Spain
[5]Research Center for Photovoltaics (RCPV), National Institute of Advanced Industrial Science and Technology (AIST),
Central 2, 1-1-1 Umezono, Tsukuba, Ibakari 305-8568, Japan

[a]Authors to whom correspondence should be addressed: Samantha.lyam@physik.uni-halle.de
and roland.scheer@physik.uni-halle.de

ABSTRACT

Hetero-junction kesterite $Cu_2ZnSn(S,Se)_4$ solar cells with low bandgap obtained from three different methods of fabrication were exposed to red light illumination, and the changes observed in their electronic properties due to this exposure were studied via open circuit voltage transients, admittance spectroscopy, capacitance voltage profiling techniques, and SCAPS simulation fits to experimental data. The results from the aforementioned techniques, in combination with temperature-dependent current voltage analysis, can be used to reveal the dominant Shockley–Read–Hall recombination path at open circuit voltage. We also derived analytical expressions for the activation energy of the saturation current density and the diode quality factor for the specific case of a solar cell device that has no type inversion at the absorber/buffer interface and is limited by interface recombination in the open circuit condition. It is found that the dominant recombination pathway for the low bandgap $Cu_2ZnSn(S,Se)_4$ solar cells under consideration is located in the space charge region and not at the absorber/buffer interface.

I. INTRODUCTION

Kesterite [$Cu_2ZnSn(S, Se)_4$] thin film solar cells are reported to have higher photovoltaic conversion efficiencies when compared with other emerging critical raw materials-free (CRM-free) technologies.[1] However, knowledge of their electronic properties is still very limited in comparison with their parent material $Cu(In, Ga)Se_2$. For the latter material, persistent photoconductivity is a well-known property giving rise to several metastabilities.[2–7]

These metastable effects, as induced in the electrical characteristics of $Cu(In,Ga)(S,Se)_2$ solar cells, can be grouped into two:[4,6,8] Light soaking (LS) effects (red, blue, and white light) and voltage-bias effects (forward or reverse bias). Red light soaking (RLS) in $Cu(In,Ga)(S,Se)_2$ is reported to induce an increase in the junction capacitance (detected by admittance spectroscopy),[7] an increase in the doping density (measured by capacitance–voltage profiling),[9] and a change (increase or decrease) in the open circuit voltage (V_{oc}).[10,11] All these effects are indicators for metastability as they are persistent at low temperature but are reversible upon sample relaxation at higher temperatures.[12] In Ref. 10, the V_{oc} metastability of $Cu(In, Ga)Se_2$ solar cells has been quantitatively related to doping density metastability. Theoretically, the V_{oc} of a solar cell has some dependence on the doping density of the absorber ($N_{A,a}$). Different recombination mechanisms, however, have different dependencies $V_{oc}(N_{A,a})$, and this provides a means to

elucidate the dominant recombination path being responsible for the limit in open-circuit voltage which otherwise is difficult to assess. In fact, the doping density metastability (red light induced) was able to reveal interface recombination in specific Cu(In,Ga)Se$_2$ devices,[13] and one may ask, is this also applicable to kesterite absorbers? Metastability effects in kesterite solar cells, induced by either light or voltage bias, are still a newly studied phenomenon.[14–17] In Refs. 15 and 18, the impact of metastability on the admittance spectra (AS) of kesterite solar cells was reported; forward bias pretreatment led to a second admittance signature and increased overall capacitance in the spectra. Single crystalline CZTSe absorber devices have also been studied via admittance, after light- (white, blue, and red light) and forward bias-induced metastability.[17] In Ref. 17, they observed metastable doping increase for white light (high), red light (higher), and forward bias (highest). Blue light [which is mostly absorbed in the buffer layer with a little penetration into the absorber (p)-buffer (n) interface] gave the lowest doping increase in contrast to red light, which penetrates deeper into the absorber. They interpreted this to mean that holes generated by blue light at the absorber interface layer with CdS recombined with electrons coming from the CdS layer. Reference 16 also reports the metastable doping increase after white, blue, and red LS with red light giving the lower doping increase. They also looked into the effects of LS on current–voltage (JV) characteristics and found evidence of enhanced recombination for blue and white LS. A comparison of JV forward current after different LS treatments showed that white light (a combination of blue and red light effect) had the highest increase followed by blue light. External quantum efficiency of a Cd-free Cu$_2$ZnSn(S, Se)$_4$ solar cell[19] and the non-ideal device behavior of Cu$_2$ZnSn(S, Se)$_4$ and Cu$_2$ZnSnGe(S, Se)$_4$[20] in relation to LS effects have been reported. To avoid complications from blue light effects such as persistent photoconductivity of the CdS layer,[21] in this study, we have employed red light soaking to limit the generation of holes to the kesterite layer and the kesterite–CdS interface.

For kesterite solar cells, the dependency $V_{oc}(N_{A,a})$ due to metastable doping increase has not yet been exploited for the detection of the dominant charge carrier recombination site at open-circuit condition; there is still an ongoing discussion on whether the small V$_{oc}$ (or high V$_{oc}$ deficit) of kesterite solar cells is due to limitations from interface recombination[22–25] or bulk recombination.[26,27] Thus, on the one hand, this article shall confirm and quantify red light effects in kesterite layers on the absorber doping density. On the other hand, the quantitative knowledge on doping metastability, in combination with the diode quality factor A and activation energy (E_A) of the saturation current density (J_o), shall be employed to investigate the dependency $V_{oc}(N_{A,a})$. The goal is to identify the dominant recombination mechanism in low bandgap kesterite solar cells. The structure of this article is as follows: Section I addresses existing findings of metastability effects in kesterite solar cells in comparison with CIG(S,Se)$_2$. It also delves into the recombination models used for the analysis of our findings. Section II explains the experimental procedures. In Sec. III, the results from experiments and analytical models are presented and compared. Section IV discusses the results and gives reasons for the exclusion of formerly discussed recombination paths. Section V gives our conclusions.

A. Open circuit voltage metastability

If the doping density in the absorber of a heterostructure solar cell is increased, depending on the dominant recombination mechanism, different trends for the V_{oc} are expected. Several of these mechanisms and their related V$_{oc}$ trends have been discussed in the literature.[10,28,29] Table I gives a summary of the formerly known[10] and newly considered mechanisms in this article, their $V_{oc}(t)$ trends, as well as their E_A and A values[12,29] as is applicable to the different regions of recombination. We can see from this table (see also Fig. 7) that upon exposure to red light, $V_{oc}(t)$ is expected to increase in the instances of space charge region (SCR) recombination (without substantial tunneling enhancement) and quasi-neutral region (QNR) recombination. Furthermore, $V_{oc}(t)$ should decrease over time for the case of an interface (IF) recombination dominated device with an inverted interface (see definition in Ref. 10). In the case of IF recombination with Fermi-level pinning, $V_{oc}(t)$ should be constant.

Physically, an increase in carrier concentration in the bulk of an absorber leads to a reduction in the absorber depletion width. Consequently, the zone of high recombination shrinks (see Appendix) and a device dominated by SCR recombination exhibits a larger V_{oc}.[3,10] In the case of dominant QNR recombination, a rising $N_{A,a}$ increases the built-in potential, also resulting in a larger V_{oc}. For dominant recombination at an inverted IF (where electrons are majority carriers in contrast to the bulk of the absorber), an increase in N$_{A,a}$ leads to a higher hole density at the interface and, thus, to an increased recombination,[3,10] consequently V_{oc} falls.[3,12] If a device shows Fermi-level pinning at the absorber/buffer IF and is limited by IF recombination, the hole density at the interface does not change upon increasing $N_{A,a}$ and V_{oc} shows no dependence on N$_{A,a}$. Furthermore, if the dominant recombination is tunneling enhanced,

TABLE I. Expected $V_{oc}(t)$ transient slopes for heterojunction thin film solar cells exposed to red light and activation energy (E_A) of J_o in comparison to the cells absorber bandgap energy ($E_{g,a}$) for different cases of Shockley–Read–Hall recombination. E_{oo} is the characteristic tunneling energy, FLP implies Fermi-level pinning, $E_{g,i}$ denotes the bandgap at the absorber/buffer interface, and ΔE_c is the conduction band offset at the buffer/absorber interface.

Recombination effect limiting V_{oc}	Activation energy of J_o (E_A)	Diode quality factor (A)	Red light $V_{oc}(t)$
QNR	$E_A = E_{g,a}$	≈1	↗
SCR (discrete defect)	$E_A = E_{g,a}$	≈2	↗
SCR ($N_d(E)$), $E_{oo} = 0$	$E_A = E_{g,a}$	1 to 2	↗
SCR ($N_d(E)$), $E_{oo} > 0$	$E_A = E_{g,a}$	1 to ≥2	E_{oo} dependent
IFR (inverted), no FLP, $\Delta E_c = 0$	$E_A = E_{g,a}$	1 to 2	↘
IFR (inverted) no FLP, $\Delta E_c < 0$ ($\Delta E_c > 0$)	$E_A < E_{g,a}$ ($E_a = E_{g,i}$)	1 to 2	↘
IF (non-inverted), no FLP	$E_A \langle or \rangle E_{g,a}$	1 to 2	↗
IF (non-inverted/ inverted), FLP	$E_A = \varphi_b^p < E_{g,a}$	≈1	⟶

V_{oc} is expected to drop with the increase in $N_{A,a}$ in the instance of interface recombination. If tunneling-enhanced SCR recombination dominates, we shall show here that $V_{oc}(N_{A,a})$ is dependent on the magnitude of the tunneling energy (E_{oo}). Hence, $V_{oc}(t)$ will rise if E_{oo} is small and will fall as predicted in Ref. 30 when E_{oo} becomes large with a higher $N_{A,a}$. This type of recombination shall also be treated in the subsequent model considerations.

Table I also lists the case of recombination at a non-inverted interface. This case is newly treated in this work. It is clear from an examination of this table that based on the expected $V_{oc}(t)$ trends alone, there is some ambiguity in the three instances, QNR, SCR, and IF (non-inverted) recombination, where for all three cases, rising V_{oc} transients should occur. Here, a consideration of the secondary parameters, such as the activation energy E_A and the diode quality factor A, may allow for differentiation between the recombination sites.

B. Model considerations

In this work, we consider two models that have yet to be analyzed in view of their specific V_{oc} ($N_{A,a}$) dependence for possible recombination mechanisms limiting V_{oc}: SCR recombination via exponentially decaying defect states with enhancement by charge carrier tunneling and IF recombination in the instance of a device structure with no type inversion at the absorber/buffer interface (referred to hereon as a non-inverted IF model). These models have been selected on the premise of the non-ideal behavior of Cu$_2$ZnSn(S,Se)$_4$ solar cells,[20] the possible existence of bandgap tail states[31] in such cells, and the information available to us from the $V_{oc}(t)$ and current voltage analysis of our Cu$_2$ZnSn(S,Se)$_4$ samples.

1. Tunneling enhanced SCR recombination model

The goal of this section is to derive an analytical expression of V_{oc} as a function of $N_{A,a}$ for the case of Shockley–Read–Hall recombination in the SCR which is enhanced by tunneling. To achieve this, we consider the equation for the diode current in the general form, assuming a high forward bias and ignoring the contribution of series and parallel resistors:

$$J_{diode} = J_o \exp\left(\frac{qV}{Ak_BT}\right). \quad (1)$$

The saturation current density J_o is given by

$$J_o = J_{oo} \exp\left(\frac{-E_a}{Ak_BT}\right), \quad (2)$$

where J_{oo} is the reference current density which is largely temperature independent. Equation (1) in the limit of SCR recombination via discrete defects takes the following form:[12]

$$J_{\text{diode}} = \frac{\pi k_B T}{2F_m} \left(\frac{N_{C,a}N_{V,a}}{\tau_{n_a}\tau_{p_a}N_{A,a}}\right)^{\frac{1}{A}} \exp\left(\frac{-E_{g,a}}{Ak_BT}\right) \exp\left(\frac{qV}{Ak_BT}\right). \quad (3)$$

Assuming an asymmetric junction, with the depletion width (W_a) mostly in the absorber, F_m (the electric field at the point of maximum recombination) can be approximated as[10,12]

$F_m \sim W_a^{-1} \sim N_{A,a}^{1/2}$ and $A = 2$ is obtained for SCR recombination via discrete defects.

Under illumination and at V_{oc}, it is $J_{diode} = 0$ and the term $-J_{ph}(V_{oc}) = -J_{sc}$ (short circuit current) can be included on the right-hand side of Eq. (3). The dependence of V_{oc} on $N_{A,a}$ for a discrete defect is arrived at by rearranging the expression to get

$$V_{oc}(N_{A,a}) = \frac{E_{g,a}}{q} + \frac{2k_BT}{q} \ln\left(\frac{2J_{sc}F_m}{\pi k_BT}\left(\frac{\tau_{n_a}\tau_{p_a}N_{A,a}}{N_{C,a}N_{V,a}}\right)^{\frac{1}{2}}\right), \quad (4)$$

where k_B denotes the Boltzmann constant, q is the elementary charge, T is the temperature, $N_{C,a}$ and $N_{V,a}$ are the conduction and valence band density of states, and τ_{n_a} and τ_{p_a} are the recombination lifetimes of electrons and holes, respectively.

Going further, consider an exponential distribution of recombination centers N_d (cm^{-3}), with maximum N_{d0} at the valence band edge (E_v) and decaying into the bandgap with characteristic energy k_BT^*. Such a defect distribution is given as[12,32,33]

$$\frac{dN_d(E)}{dE} = \frac{N_{do}}{k_BT^*} \exp\left(\frac{-(E - E_v)}{k_BT^*}\right), \quad (5)$$

where E denotes the variable in the distribution. For recombination via such a defect distribution in the SCR with tunneling enhancement, the reference current density is expressed as[12,33]

$$J_{\text{diode}} = 2\sqrt{3}\pi\frac{k_BT}{F_\Gamma}\left(\frac{N_{c,a}N_{v,a}}{\tau_{p,a}\tau_{n,a}}\right)^{1-\Xi/2}\left(\frac{\tau_{p,a}N_{c,a}}{\tau_{n,a}N_{v,a}}\right)^{T/2T^*}\left(\frac{N_{A,a}}{\tau_{P_a}}\right)^{\Xi}$$
$$\wedge(T/T^*, 1+\Xi)\exp\left(\frac{qV - E_{g,a}}{Ak_BT}\right). \quad (6)$$

In Eq. (6), one can identify J_{oo} as

$$J_{oo} = 2\sqrt{3}\pi\frac{k_BT}{F_\Gamma}\left(\frac{N_{c,a}N_{v,a}}{\tau_{p,a}\tau_{n,a}}\right)^{1-\Xi/2}\left(\frac{\tau_{p,a}N_{c,a}}{\tau_{n,a}N_{v,a}}\right)^{T/2T^*}\left(\frac{P_a}{\tau_{P_a}}\right)^{\Xi}\wedge(T/T^*, 1+\Xi), \quad (7)$$

where $F_\Gamma = [24m^*(k_BT)^3]^{1/2}/q\hbar$ is the characteristic tunneling electric field strength with m^* representing the effective tunneling mass. $N_{A,a}$ is the hole concentration in the absorber bulk. The function $\wedge(T/T^*, 1+\Xi)$ denotes an integral term[33] that can be solved numerically. Its dependence on the normalized temperature T/T^* for different values of E_{oo}/k_BT^* can be found in Ref. 32. The character Ξ is given as $\Xi = E_{oo}^2/3(k_BT)^2$, where E_{oo} is the characteristic tunneling energy expressed as[34]

$$E_{oo} = \left(\frac{q\hbar}{2}\right)\left(\frac{N_{A,a}}{m^*\varepsilon_a}\right)^{\frac{1}{2}}, \quad (8)$$

with ε_a representing the dielectric constant of the absorber material. We will show in Sec. III that $V_{oc}(N_{A,a})$ is dependent on the magnitude of the characteristic tunneling energy E_{oo}. In Eq. (6), the condition $(1+\Xi)\tau_{n_o,a}p = (1-\Xi)\tau_{p_o,a}n$ defines the local maximum of the recombination rate. Hence, from Eq. (6), the diode quality

factor for tunneling-enhanced SCR recombination via $N_d(E)$ comes out as

$$\frac{1}{A} = \frac{1}{2}\left(1 + \frac{T}{T^*} - E_{oo}^2/3(k_BT)^2\right). \quad (9)$$

In the limit $E_{oo} \to 0$ (i.e., without tunneling contributions), J_{00} and A revert to[32]

$$J_{oo} = \frac{k_BT}{F_m}\left(\frac{N_{c,a}N_{v,a}}{\tau_{p,a}\tau_{n,a}}\right)^{1/A}\left(\frac{\tau_{p,a}^2}{N_{v,a}^2}\right)^{T/2T^*} \wedge (T/T^*, 1)$$

and

$$\frac{1}{A} = \frac{1}{2}\left(1 + \frac{T}{T^*}\right). \quad (10)$$

Furthermore, in the limit $T^* \to 0$ another scenario; tunneling-enhanced SCR recombination via a discrete defect is possible. The diode quality factor in such an instance is given as

$$\frac{1}{A} = \frac{1}{2}(1 - E_{oo}^2/3(k_BT)^2). \quad (11)$$

Now, to arrive at the dependency $V_{oc}(N_{A,a})$ for tunneling-enhanced SCR via $N_d(E)$, we take into account that the reference current density for such a scenario can have two contributions. The recombination rate[35] can consist solely of the standard SRH recombination, in which case J_{oo} is given by Eq. (10),[32] or it can have an additional contribution from tunneling enhancement as is in Eq. (7).[32] We therefore calculated $V_{oc}(N_{A,a})$ for tunneling-enhanced SCR via $N_d(E)$ numerically because there is no closed analytical expression for $V_{oc}(N_{A,a})$ from Eq. (7).

2. Interface recombination IFR model

In the case of a device limited by IF recombination, the function $V_{oc}(N_{A,a})$ depends on the energy band diagram. In order to arrive at an expression for a non-inverted absorber/buffer, we have followed the procedure laid down for the inverted case in Ref. 29. Neglecting tunneling enhancement effects at the inverted interface, the diode current is given as[12,29]

$$J_{diode}^{IF} = qS_pN_{V,a}\exp\left[\frac{-E_{p,a}^{IF}(V)}{k_BT}\right], \quad (12)$$

where $E_{p,a}^{IF}(V)$ is the hole barrier at the interface and S_p is the surface recombination velocity. Equation (12) means that the availability of holes limits the recombination current at an inverted interface. When we allow the charged acceptor interface states N_t^{IF} in unit of cm^{-2}, $E_{p,a}^{IF}(V)$ takes on the form

$$E_{p,a}^{IF}(V) = E_{p,a}^{QNR} + qV_{bi} - qV + \Delta\chi + \frac{q^2N_{D,b}d_b^2}{2\varepsilon_b} + \frac{q^2\varepsilon_aN_{A,a}d_b^2}{\varepsilon_b^2} - \frac{d_bN_t^{IF}q^2}{\varepsilon_b} - \frac{d_bN_{A,a}q^2}{\varepsilon_b}\sqrt{\frac{2\varepsilon_a}{q^2N_{A,a}}\left(q(V_{bi}-V) + \frac{q^2d_b^2N_{D,b}}{2\varepsilon_b} - \frac{q^2d_bN_t^{IF}}{\varepsilon_b}\right) + \frac{d_b^2\varepsilon_a^2}{\varepsilon_b^2}}. \quad (13)$$

This expression is valid for an inverted and a non-inverted absorber. In Fig. 1(a), we see that the Fermi level for the non-inverted absorber is below midgap at equilibrium. This is an indication that at a non-inverted interface, holes are the majority carriers. Therefore, J_{diode}^{IF} for a device with a non-inverted interface will take on the form

$$J_{diode}^{IF} = qS_nN_{C,a}\exp\left[\frac{-E_{n,a}^{IF}(V)}{k_BT}\right], \quad (14)$$

where $E_{n,a}^{IF}(V)$ is the electron barrier height at the interface expressed as $E_{n,a}^{IF}(V) = E_{g,a} - (qV + E_{p,a}^{IF}(V))$ and S_n is the surface recombination velocity for electrons. Using Eq. (13), we get

$$E_{n,a}^{IF}(V) = E_{g,a} - qV_{bi} - E_{p,a}^{QNR} - \Delta\chi - \frac{q^2N_{D,b}d_b^2}{2\varepsilon_b} - \frac{q^2\varepsilon_aN_{A,a}d_b^2}{\varepsilon_b^2} + \frac{d_bN_t^{IF}q^2}{\varepsilon_b} + \frac{d_bN_{A,a}q^2}{\varepsilon_b}\sqrt{\frac{2\varepsilon_a}{q^2N_{A,a}}\left(q(V_{bi}-V) + \frac{q^2d_b^2N_{D,b}}{2\varepsilon_b} - \frac{q^2d_bN_t^{IF}}{\varepsilon_b}\right) + \frac{d_b^2\varepsilon_a^2}{\varepsilon_b^2}}, \quad (15)$$

where $N_{D,b}$, d_b, and ε_b represent the doping, thickness, and permittivity of the buffer layer, respectively. $\Delta\chi = \Delta E_c^{a,b} + \Delta E_c^{b,w}$ balances the conduction band offsets at the buffer/absorber and window/buffer interfaces [see the inset in Fig. 1(b)]. We consider here the case of a conduction band spike with $\Delta E_c^{b,a} = -\Delta E_c^{w,b}$. Looking at Eqs. (13) and (15), we can see that J_{diode}^{IF} exhibits its voltage dependence in a square root term. Hence, to obtain E_A of J_o and A, Eq. (15) has to be linearized. Similar to the linearization in Ref. 29, this has been accomplished for Eq. (13) and in the supplementary material for Eq. (15). We then derive A for a non-inverted interface hetero-structure with acceptor states at the interface from the voltage-dependent quantities of the linearized electron barrier $E_{n,a}^{IF}(V)$ in Eq. (S6) in the supplementary material as
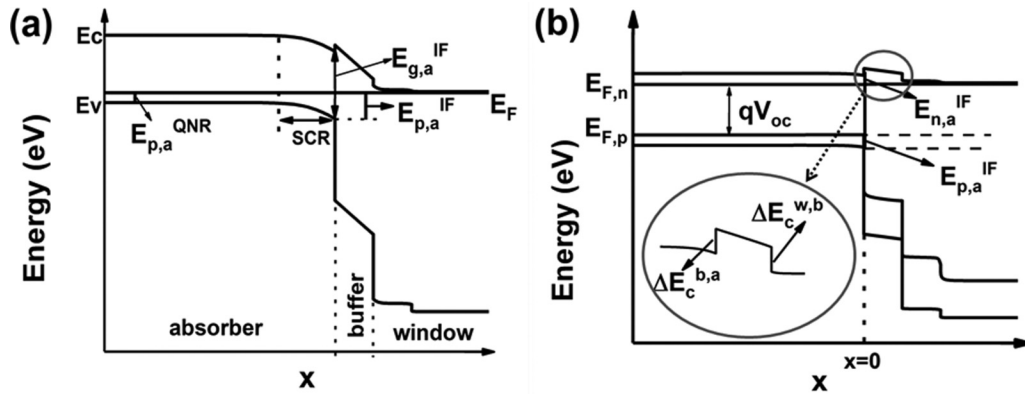
FIG. 1. Band diagram of a hetero-structured solar cell with a non-inverted absorber/buffer interface (a) in equilibrium and (b) under open circuit.

$$A_{\text{non-inverted}}^{IF} = \frac{\varepsilon_b}{d_b \varepsilon_a} \sqrt{\frac{\varepsilon_a}{q N_{A,a} \varepsilon_b^2}(d_b^2 q(\varepsilon_a N_{A,a} + N_{d,b}\varepsilon_b) + 2(V_{bi} - V_{oc})\varepsilon_b^2 - 2 d_b N_t^{IF} q\varepsilon_b)}. \tag{16}$$

The activation energy of the diode saturation current is derived from the temperature independent quantities of $E_{n,a}^{IF}(V)$ in Eq. (S6) in the supplementary material as

$$E_A^{\text{non-inverted IF}} = qV_{oc} + \frac{A^2 d_b^2 N_{A,a} q^2 \varepsilon_a}{\varepsilon_b^2} + \frac{A(2 d_b N_t^{IF} q^2 \varepsilon_b - 2(-E_{g,a} + E_{p,a}^{QNR} + qV_{bi})\varepsilon_b^2)}{2\varepsilon_b^2} - \frac{A d_b^2 q^2(2 N_{A,a}\varepsilon_a + N_{d,b}\varepsilon_b)}{2\varepsilon_b^2}, \tag{17}$$

with $A = A_{\text{non-inverted}}^{IF}$. Assumptions made for this derivation include the complete depletion of the buffer layer, no grading of the Fermi level within all the layers, the window doping is far greater than both absorber doping and buffer layer doping ($N_{D,w} \gg N_{A,a}, N_{D,b}$), and lastly, the hole concentration at the absorber-buffer interface is far greater than the electron concentration (i.e., $p_{a,IF} \gg n_{a,IF}$).

At open circuit, $J_{diode} = 0$, $V = V_{oc}$ and Eq. (14) can be written as

$$J_{sc} = q S_n N_{c,a} \exp\left(\frac{-E_{n,a}^{IF}(V)}{k_B T}\right). \tag{18}$$

An expression for $V_{oc}^{\text{non-inverted IF}}(N_{A,a})$ can be obtained by the substitution of Eq. (15) into Eq. (18) and then re-arranging the latter,

$$V_{oc}^{\text{non-inverted IF}}(N_{A,a}) = \frac{E_{g,a} - E_{p,a}^{QNR} + k_B T \log\left[\frac{J_{sc}}{N_{c,a}q S_n}\right]}{q} - \frac{\left(d_b^2 N_{d,b}q^2 + 2(-E_{g,a} + E_{p,a}^{QNR} + qV_{bi})\varepsilon_b + 2 d_b N_t^{IF}q^2 - 2k_B T\varepsilon_b \log\left[\frac{J_{sc}}{N_{c,a}q S_n}\right]\right)^2}{8 d_b^2 q^3 \varepsilon_a N_{A,a}}. \tag{19}$$

If we let

$$Y = \frac{E_{g,a} - E_{p,a}^{QNR} + k_B T \log\left[\frac{J_{sc}}{N_{c,a}q S_n}\right]}{q}$$

and

$$X = \frac{\left(d_b^2 N_{d,b}q^2 + 2(-E_{g,a} + E_{p,a}^{QNR} + qV_{bi})\varepsilon_b + 2 d_b N_t^{IF}q^2 - 2k_B T\varepsilon_b \log\left[\frac{J_{sc}}{N_{c,a}q S_n}\right]\right)^2}{8 d_b^2 q^3 \varepsilon_a},$$

then we can write Eq. (19) in the form

$$V_{oc}^{\text{non-inverted IF}}(N_{A,a}) = Y - \frac{X}{N_{A,a}}. \qquad (20)$$

From Eq. (20), we see that V_{oc} is expected to increase with the increase in $N_{A,a}$ for recombination at a non-inverted interface. Hence, one would expect a rising V_{oc} transient if a device has no type inversion at the interface and is limited by IF recombination.

II. EXPERIMENTS

A. Samples

We investigated solar cells from three research institutes: Laboratory for Thin Films and Photovoltaics (EMPA)—Swiss Federal Laboratories for Materials Science and Technology, Switzerland, Research Center for Photovoltaics (RCPV)—National Institute of Advanced Industrial Science and Technology (AIST), Tsukuba, Japan, and The Catalonia Institute for Energy Research (IREC), Spain. EMPA samples are solution-processed kesterites with a device structure: soda lime glass (SLG)/SiO$_2$ (diffusion barrier)/molybdenum (1 μm)/Li alloyed (1 at. %)CZTSSe (1.5 μm)/CdS (50 $-$ 70 nm)/i $-$ ZnO/Al $-$ ZnO (70 nm/250 nm)/ Ni $-$ Al (top grid)/MgF$_2$ anti-reflective coating. The CZTSSe precursor solution was spin coated on top of the molybdenum layer and dried on a hot plate in air. More details of the EMPA sample fabrication can be found in Ref. 36. IREC, on the other hand, produced their kesterite absorber by the deposition of metal stacks of Cu, Sn, and Zn using dc magnetron sputtering. After this, a rapid thermal annealing process (RTP) in a Se–Sn atmosphere was performed to obtain high quality CZTSe layers. IREC's solar cell structure is SLG/Mo/CZTSe ($\sim$2 μm)/CdS(50 nm)/i $-$ ZnO(50 nm)/ In$_2$O$_3$:SnO$_2$(ITO)(200 nm)/Ni $-$ Al top grid. Further details of the IREC procedure can be found in Ref. 37. Lastly, the AIST sample that is also a pure selenium kesterite solar cell had its absorber layer deposited on a molybdenum-coated soda lime glass via co-evaporation of the elements Cu, Zn, Sn, and Se using molecular beam epitaxy. After deposition, a thermal annealing treatment is performed under a flow of an evaporated mixture of SnSe$_2$ and N$_2$ gases in a furnace tube. AIST's solar cell structure is SLG/Mo/CZTSe (1.8 μm)/CdS(50 nm)/ i $-$ ZnO (50 nm)/Al $-$ ZnO(350 nm). More details on their deposition procedure can be found in Ref. 24. Each sample solar cell is bonded from the front and back contacts to the contact side of the sample holder with gold wires (35 μm thin). All three solar cells have a low bandgap around 1 eV (see Table II).

B. Definition of the sample state

In order to define the relaxed state of the kesterite absorber, the samples were mounted on a heating–cooling Peltier stage in a light-tight vacuum chamber and stored in the dark chamber for a minimum of 16 h at a temperature of 318 K. From monitoring of capacitance–frequency spectra after relaxation and red light soaking, we observe that relaxation already starts to take place at temperatures $\geq$270 K. Above 270 K, the overall capacitance measured begins to decline if light soaking is not done in between temperature steps.

TABLE II. Summary of the experimental results for EMPA, IREC, and AIST samples.

Cell type	EMPA (CZTSSe)	IREC (CZTSe)	AIST (CZTSe)
Efficiency (%)	10	6	10
V_{OC} (mV)	518	404	387
FF	60	48	61
J_{SC} (mA cm^{-2})	35	32	37
$E_{g,a}$ (eV)	1.1 (1.0)	1.1 (1.0)	1.0 (0.9)
$E_{A,0}$ (eV)	1.1 $\pm$ 0.03	1.4 $\pm$ 0.10	1.2 $\pm$ 0.1
J_{oo} (mA cm^{-2})	$(6 \pm 3) \times 10^5$	$(4 \pm 3) \times 10^8$	$(1.2 \pm 0.1) \times 10^9$
Relaxed $N_{A,a}$ (cm^{-3})	7×10^{15}	2×10^{15}	2×10^{15}
RLS $N_{A,a}$ (cm^{-3})	8×10^{16}	4×10^{15}	1×10^{16}
Relaxed Dark A (300 K)	1.5	1.9	1.4
RLS Dark A (300 K)	1.3	1.8	1.3
RLS Light A (300 K)	1.3	1.9	1.2
Relaxed C_{SCR} (nF cm^{-2})	19	13	19
RLS C_{SCR} (nF cm^{-2})	76	21	47
Relaxed V_{bi} (V), RLS V_{bi} (V)	0.8, 0.9	0.8, 0.9	0.8, 0.8
2 h RLS experimental ΔV_{OC} (mV)	32	52[a]	24

[a]The ΔV_{oc} recorded for the IREC sample is inclusive of V_{oc} increase due to cell recovery from other anomalies brought on by relaxation.

Elevating the sample temperature in the dark to 318 K further enhances the relaxation process. We found that a wait period of 16 h at 318 K is sufficient to achieve a relaxed state. For our samples, a relaxed state is characterized by doping density levels in the range of 10^{15} cm^{-3} and a V_{oc} less than the optimum of the cells by 10 mV or more. The optimum V_{oc} is recovered upon exposure to white light. To secure relaxed or metastable sample states for experiments, a vacuum chamber is fitted to a sun simulator calibrated to generate AM 1.5 G illumination. A light-tight shutter outside the vacuum chamber allows the accurate definition of the illumination period. Red light illumination is realized by a long pass filter with cut off wavelength of 590 nm (2.1 eV) placed inside the vacuum chamber in the light path of the sun simulator. After opening the light shutter, the samples are in a transient state, which are sampled in the $V_{oc}(t)$ measurements. For admittance spectroscopy and capacitance–voltage profiling measurements in the red-light soaked state (RLS), the samples were illuminated in the vacuum chamber with red light for 2 h at a temperature of 300 K. Then, the temperature was lowered to the desired temperature for measurement with the illumination still on. The illumination was left on while cooling down or increasing the temperature to avoid relaxation of metastable states while in the dark. It was put off upon attainment of the desired temperature to allow for temperature stabilization. Then, the admittance or capacitance measurement was performed in the dark.

C. Admittance spectroscopy

This experiment was conducted in the same chamber as stated above. In this case, however, the sample holder was mounted onto a cryostat head. At the start of the experiment, the dark chamber is pumped to high vacuum of approximately 4×10^{-5} mbar and then the temperature of the sample is lowered with the aid of a closed cycle two-stage helium cryostat. The temperature range used for our measurements was 110–300 K with a temperature step size of 10 K. No voltage-dependent measurements were performed on relaxed samples prior to taking the admittance measurement in order to avoid excitation of a metastable state. In the RLS state, the admittance measurement was conducted from low to high frequency with the same temperature range and step size as in the relaxed state. Again, in order to avoid relaxation of the metastable state with the increase in temperature, the illumination was put back on for every temperature step increase and put off before measurement. An Agilent E4980A LCR-meter using a test voltage of 50 mV was used to measure the capacitance variation with frequency. In addition, voltage-dependent admittance spectroscopy was done in a selected temperature range (150–230 K) to investigate possible interface defects.[28] An external dc voltage bias range (of −0.8 to 0.4 V for EMPA and AIST samples, and −0.8 to 0.25 V for the IREC sample) was applied and left on for all three samples while taking the admittance measurement. This was applied in both relaxed and RLS states of the samples.

D. Capacitance–voltage profiling

DLCP measurements were carried out for the sample set at an appropriate temperature and frequency as inferred from the results of their individual admittance spectra.[38] This was carried out to estimate the absorber doping density $N_{A,a}$. In the results section of this work, the temperature–frequency combinations are represented as gray circles in Fig. 2, and they are also stated in the caption of Fig. 3. An Agilent E4980A LCR-meter was used to record DLCP profiles with an AC bias range of 0.05 V_{rms} to 0.25 V_{rms} and DC voltage ranges of −0.8 to 0.5 V for EMPA sample, −0.8 to 0.4 V for AIST, and −0.8 to 0.25 V for IREC.

E. Open circuit voltage transient $V_{oc}(t)$

The $V_{oc}(t)$ measurement itself is conducted at 298 K. Opening the light shutter starts the $V_{oc}(t)$ measurement. The V_{oc} recording is carried out by a Keithley 2400 digital source meter unit programed to measure V_{oc} after every 2 s. We performed a voltage-temperature correction after the measurement to account for the error introduced by temperature fluctuations at the start of the experiment. $\Delta V_{oc}(t)$ was referenced to the first V_{oc} measurement after the light shutter opened. It was 2 s for EMPA and AIST samples, while IREC is referenced to 30 s. More details of our V_{oc} transient measurement can be found in Ref. 39.

F. Current–voltage JV characteristics

Current–voltage analysis with temperature variation was performed using a Keithley 2400 digital source meter unit and a cryostat for the extraction of the diode quality factor (A) and the activation energy of $J_o(E_A)$. Both dark and illuminated (1 sun) JV

curves were measured in a temperature range of 120–300 K. We also varied the illumination intensity (within the vicinity of 1 sun) at 300 K in order to determine the collection efficiency and calculate the saturation current density J_o and the diode quality factor using the procedure laid out in Ref. 40.

G. External quantum efficiency (EQE)

The external quantum efficiency (EQE) was measured using a xenon lamp dispersed by a monochromator and chopped at 278 Hz in conjunction with a low noise current–voltage pre-amplifier and a lock-in amplifier. Results from this measurement were used to determine the absorber bandgap and the active area of the measured solar cells.

III. RESULTS

A. Temperature dependent Admittance Spectroscopy (TAS)

Figure 2 shows the admittance spectra for three cells measured under two conditions: Relaxed state (left) and after 2 h of red light soaking (RLS) (right). We observe that the measured capacitance at high frequency ($1 \times 10^5 - 1 \times 10^6$ Hz) reduces to geometric capacitance C_{geo} (indicated in the figure by a gray solid line) for both states of each cell. The carrier freeze out phenomenon at relatively low frequency is in agreement with other measurements of admittance spectra for kesterite solar cells.[31,41,42] With C_{geo} occurring in the frequency range of the measurement, we are able to estimate the dielectric constant for each absorber using the expression $C_{geo} = \varepsilon_r \varepsilon_o / d$, where d denotes the absorber thickness. The C_{geo} values obtained for each cell are displayed in Fig. 2. The EMPA sample has a sulfur content of <5 at. % and is alloyed with lithium (∼1 at. %); hence, it has a lower dielectric constant ε_r compared to IREC and AIST samples that are pure selenium-based kesterites (CZTSe). The ε_r value obtained for the EMPA sample falls within the theoretical values reported for CZTSSe (6.7–8.5[41]). Other works[43,44] have also reported higher ε_r values for CZTSe in comparison to CZTSSe as a resultant effect of its lower bandgap. Furthermore, the existence of voids in the absorber material could also contribute to the disparity we see in the ε_r values.

Comparing the relaxed and the RLS states of the samples as presented in the figure, we observe a capacitance step for both states, occurring around 160–230 K, which fades into the geometric capacitance at high frequency. In the RLS state, this main capacitance step is larger and higher capacitance values are recorded in the low frequency range ($1 \times 10^2 - 1 \times 10^5$ Hz). We regard this capacitance step as the main capacitance step. Its provenience currently is unknown and could lie in a defect state or a transport barrier. For each sample in the relaxed state, the main capacitance step is the only one observed. For the RLS state, however, a slight shoulder/bump at mid-frequency, mid-temperature appears in the admittance spectra. This shoulder is most pronounced for EMPA and AIST samples and is best seen in the plots of $\frac{dC}{d\omega}\omega \frac{1}{k_B T}$ against E_d in Fig. S8 in the supplementary material. Such a second admittance signature was also found in Refs. 18 and 16. Furthermore, we observe that all cells show capacitance contributions from deep defects. This is indicated from the C(f) slope in the high
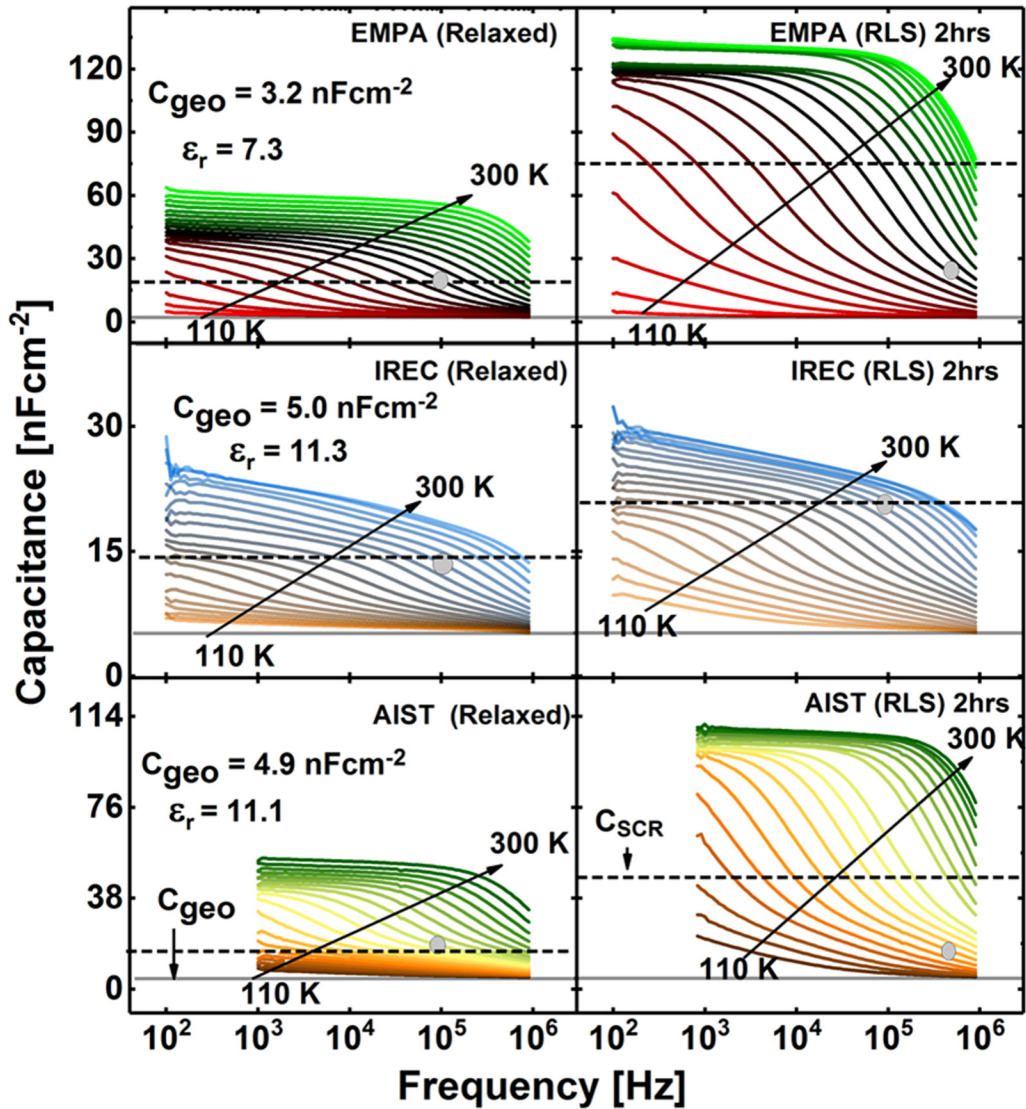
FIG. 2. Admittance spectra for the relaxed (left) and red light soaked (RLS) states (right) of EMPA, IREC, and AIST solar cells. The gray circles indicated in the plots represent the temperature–frequency combination used for DLCP measurements. The dashed lines correspond to the calculated values of the respective space charge region capacitance (C_{scr}). The full lines indicate the calculated geometrical capacitance value. Note the difference in scale on the capacitance axis for the respective samples.

temperature–low frequency range. It is most pronounced in the case of the IREC sample.

In order to confirm if interface states contribute to the measured capacitance seen in Fig. 2, we carried out voltage-dependent admittance measurements for each cell.[45] From this, we obtained the activation energies of the admittance signature as a function of voltage in the temperature range 150–230 K (Fig. S9 in the supplementary material). Biasing a solar cell varies the position of the quasi-Fermi levels at the interface. The point at which one of the quasi-Fermi levels intersects a defect energy level determines the activation energy of such a defect. The activation energy can be

obtained from an Arrhenius plot of $\ln\left(\frac{\omega_o}{T^2}\right)$ $(s^{-1}K^{-2})$ against $\left(\frac{1}{T}\right)k_B$ (eV) that comes from the following relation:

$$\omega_o = N_{C,V}\nu_{th}\sigma_d T^2 \exp\left(-\frac{E_d}{k_B T}\right) = 2\xi_o T^2 \exp\left(-\frac{E_d}{k_B T}\right), \quad (21)$$

where ω_o is the inflection frequency of the capacitance–frequency curve (the maximum point of $-\omega dC/d\omega$ vs ω plot), ξ_o is the thermal exponential pre-factor (attempt to escape frequency), ν_{th} is the thermal velocity of carriers, σ_d is the defect capture cross

section, $N_{C,V}$ is the effective density of states in the conduction or valence band of the absorber, and E_d is the defect activation energy. The results we obtained are shown in Fig. S9 in the supplementary material. We observe that for each cell, the activation energy (E_d) changes to lower energy levels after RLS. However, for all three samples, E_d is not voltage dependent.

B. Capacitance–voltage profiling

All measured samples displayed in Fig. 2 show an increase in capacitance after RLS. Unfortunately, it is not possible to extract the value of the space charge region capacitance C_{scr} directly from the admittance spectra since additional phase-shifting elements such as defects (in parallel to the junction) or a barrier (in series) may contribute to the TAS plot. Hence, we have performed drive-level capacitance (DLCP) measurements at selected intermediate temperatures. These temperatures need to be high enough to avoid the influence of the carrier freeze out that results in C_{geo} in the admittance spectra and to minimize the contribution of a possible back contact barrier. They need to be low enough to minimize the influence of deep defects. The frequency for the DLCP measurement was chosen in like manner; around the inflection point of the admittance spectrum for the selected temperature to minimize the contribution of deep defects to the junction capacitance. The DLCP measurement conditions are indicated on the selected admittance spectrum as small gray circles (see Fig. 2).

The results displayed in Fig. 3 are the apparent doping densities ($N_{A,a}$) obtained from DLCP measurements of EMPA, IREC, and AIST cells, respectively. It can be observed that for all three cells that there is an increase in $N_{A,a}$ in the RLS state compared to their relaxed state. We also observe that after RLS, the space charge region width (w_a) shrinks [Figs. 3(a) and 3(c)], similar to the results obtained by Refs. 16 and 17. There is also a rise in $N_{A,a}$ in forward bias (smaller $\langle x \rangle$) for the cases of EMPA and AIST RLS states. In contrast, for the IREC sample, the increase in $N_{A,a}$ occurs in the reverse bias region for both cases of relaxed and RLS states. Although being subject to large errors, both the admittance and DLCP measurements indicate that there is an increase in capacitance/doping for all investigated cells with the stronger effect seen for the EMPA and AIST samples. Due to the non-uniformity of

these doping profiles, the zero bias point of the profile in the case of IREC and AIST (both states) and for EMPA (relaxed state) as listed in Table II are used for the analysis. For EMPA RLS state, however, the $N_{A,a}$ profile is very close to the p–n interface and does not have the U shape. This could be due to a higher doping of the absorber layer in comparison to the buffer layer. In this case, there would be a larger potential drop over the buffer layer; the p–n junction is no longer an ideal one-sided junction (see Ref. 12, p. 24). Hence, to approximate doping in the absorber, the lowest point of the profile (corresponding to extreme reverse bias) is listed in Table II for the EMPA RLS state. The space charge capacitance C_{scr} for both states of each cell was calculated using the following expression:

$$C_{scr} = \sqrt{\frac{\varepsilon_a q N_{A,a}}{2 V_{bi}}}. \qquad (22)$$

The resulting C_{scr} values have been indicated in Fig. 2 as black dashed lines. We see that C_{scr} increases after RLS for all three samples. This is an indication that there is additional charge in the SCR upon exposure to red light which leads to a reduction of the SCR width seen in Figs. 3(a) and 3(c). Since deep defects or a back barrier can influence the slope of a Mott–Schottky plot from C–V measurements, the built-in voltage V_{bi} in Eq. (22) was calculated from the following expression:[29]

$$V_{bi} = E_{g,a} - E_{p,a} - \Delta\chi - E_{n,w}$$
$$= \left(E_{g,a} - k_B T \left(\ln \left(\frac{N_{V,a} N_{D,w}}{N_{C,w} N_{A,a}} \right) \right) \right) \Big/ q. \qquad (23)$$

In Eq. (23), we used the values of doping density of the window layer ($N_{D,w}$) as given in literature[12,46] for Al:ZnO layers (1×10^{18}) and for Sn:In$_2$O$_3$ (1×10^{19}) to calculate the Fermi-level position $E_{n,w}$. $\Delta\chi$ was assumed to be zero. The $N_{A,a}$ was taken from Fig. 3 at the lowest point of each curve for the calculation of the hole quasi-Fermi level in the bulk $E_{p,a}$. We have confirmed our DLCP $N_{A,a}$ results with C–V measurements (not shown here) conducted on the same samples for various temperature and frequency combinations.[47,48]
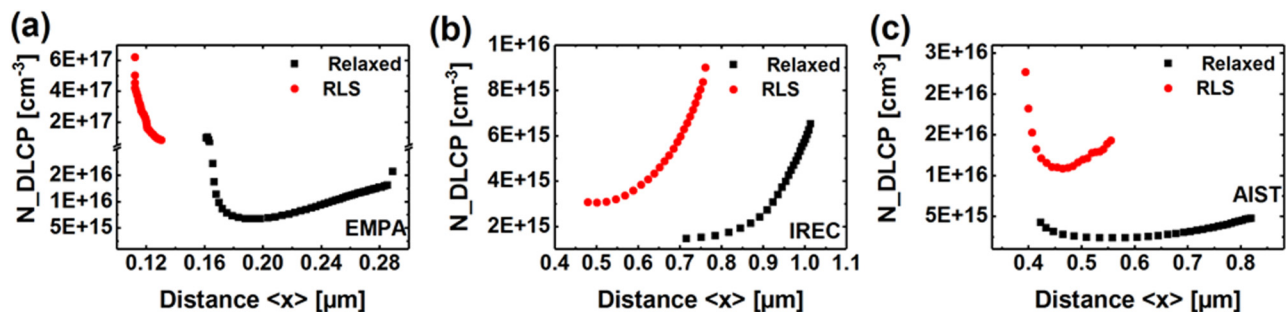

FIG. 3. The apparent doping densities as obtained from DLCP measurements for (a) EMPA cell at 200 K, in relaxed and red light soaked state (100 and 500 kHz, respectively), (b) IREC cell, both states (250 K, 100 kHz). (c) AIST cell, relaxed (200 K, 100 kHz) and RLS state (200 K, 500 kHz).

C. Open circuit voltage transients $\Delta V_{oc}(t)$

Knowing that doping in all investigated samples increases upon RLS, in agreement with Refs. 14, 16, and 17, it is postulated that this doping increase influences the devices' V_{oc}. Accordingly, the time-transient of V_{oc} upon light exposure after sample relaxation have been measured. Figure 4 shows the change in V_{oc} with time upon exposure to red light. For all three samples, we see a rising trend for ΔV_{oc}, similar to what has been reported for some low gallium Cu(In, Ga)Se$_2$ solar cells.[3,9,10,49] The relative change in V_{oc} is similar for the EMPA and AIST sample but is larger for the IREC sample. The $\Delta V_{oc}(t)$ axis in Fig. 4 is referenced as $\Delta V_{oc}(t) = V_{oc}(t) - V_{oc}$ (2 s) for EMPA and AIST. For IREC, it is $\Delta V_{oc}(t) = V_{oc}(t) - V_{oc}$ (30 s). The $\Delta V_{oc}(t)$ increase obtained at V_{oc} ($t = 7200$ s) for each sample amounts to 32, 52, and 24 mV for EMPA, IREC, and AIST respectively. Although the IREC sample shows a higher V_{oc} increase, we note here that this sample has a poor response to red light after relaxation. The measured V_{oc} amounted to only 100 mV under red light but recovers to 404 mV under white light. We speculate that this anomaly is related to an additional phenomenon to metastable doping increase, but this needs further investigation. Nevertheless, the IREC sample (like EMPA and AIST) shows an increase in V_{oc} with time after relaxation. The V_{oc} range measured and used for calculation of $\Delta V_{oc}(t)$ for each of the samples is 470–502 mV for EMPA, 49–101 mV for IREC, and 364–388 mV for AIST. The time dependence of V_{oc} for all samples may be described by a power law of type $V_{oc}(t) = V_{oc}^0 \left(1 + \frac{t}{t_c}\right)^\beta$, similar as reported for Cu(In, Ga)Se$_2$ devices in Ref. 10.

D. JV and EQE analysis

1. Diode quality factor (A) and activation energy (E_A) of the saturation current density

In order to determine device parameters such as activation energy of the saturation current density (E_A) and diode quality factor (A), dark JV curves of the samples were measured after sample relaxation and analyzed in the temperature interval $200 - 300$ K according to the procedure laid out in Ref. 50 (see Figs. S2–S4 in the supplementary material). Light and dark JV curves were also measured after 2 h of red light soaking (RLS) and were fitted to obtain A in the RLS state (Fig. S5 in the supplementary material). The fit results can be seen in Tables S1–S3 in the supplementary material
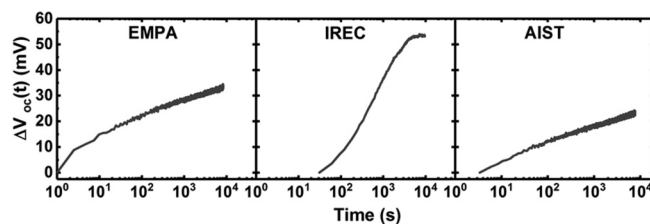

FIG. 4. Variation of open circuit voltage with time of EMPA, AIST, and IREC cells exposed to red light at 300 K after 16 h of relaxation in the dark at 318 K.

together with the obtained series resistance R$_s$ and shunt conductance G$_{sh}$. Table II shows the A factor values of the three samples at 300 K in the dark relaxed, dark RLS, and light RLS states. The A factor values at room temperature for EMPA and AIST samples are far less than two, while for the IREC sample, A is close to 2. The activation energy (E_A) of the saturation current density J_o and the reference current density J_{oo} were extracted from the temperature-dependent quantities $A(T)$ and $J_o(T)$ using the method proposed by Hages et al. in Ref. 20. Here, the activation energy was allowed to be temperature dependent according to $E_A = E_{A,0} - \alpha T$, where $E_{A,0}$ is the activation energy at zero Kelvin and αT accounts for temperature-dependent energy bandgap $E_{g,a}(T)$ and potential fluctuations.[20] The plots from this method can be found in Fig. S6 in the supplementary material. In the temperature range of 280–306 K, we obtained for the EMPA sample $\alpha = 0.6 \pm 0.1$ meV K^{-1} and $J_{oo} = 6 \times 10^5 \pm 3 \times 10^5$ mA cm^{-2}. These values are in the range of the result for the CZTSSe solar cell published in Ref. 20. The IREC and AIST that are CZTSe samples (that is pure Se kesterite) were derived as $\alpha = 0.5 \pm 0.3$ meV K^{-1}, $J_{oo} = (4.3 \pm 3.8) \times 10^8$ mA cm^{-2} and $\alpha = 0.5 \pm 0.2$ meV K^{-1}, $J_{oo} = 1.2 \pm 0.1 \times 10^9$ mA cm^{-2}, respectively. These α values can be attributed to the presence of potential fluctuations and a temperature dependent absorber bandgap.[20] For the activation energy of J_0 at 0 K, we find in the temperature range of 280–306 K, $E_{A,0\_EMPA} = 1.1$ eV, $E_{A,0\_IREC} = 1.4$ eV, and $E_{A,0\_AIST} = 1.2$ eV.

2. Defect distribution in the space charge region and tunneling-enhanced recombination

Figure 5 gives the temperature dependence of the inverse of A (from fits to dark JV data of relaxed samples). We find an increase in the value of A with the decrease in temperature, with A exceeding 2 below 260 K for the IREC sample and below 210 K for the AIST sample, depicted by the falling $1/A$ values with decreasing temperature. As is given by Eqs. (9) and (10), such a dependence of A on temperature can be attributed to the existence of tail states in the bandgap of a device and possible tunneling contributions. The fits in plots Fig. 5(a) were performed with Eq. (9) (tunneling-enhanced recombination over defect distribution) and Fig. 5(b) with Eq. (10) (recombination over defect distribution). These fits yield the values of E_{oo} and T^* displayed from which we calculate the characteristic energies of $k_B T^* = 60$ and 37 meV for IREC and AIST samples, respectively. From the $k_B T^*$ values of the samples, a quantitative understanding of how deep the defect distribution decays into the region of efficient recombination in the SCR can be reached (see Ref. 12, p. 54). The application of Eq. (8) reveals that the E_{oo} values obtained from the fits in Fig. 5(a) can only be realized with $N_{A,a}$ of the order of 10^{18} cm^{-3}. Compared to $N_{A,a}$ estimated from the experiment for these samples, these E_{00} values are too high. We therefore consider that for all three samples, an increase in series resistance R$_s$ below 260 K was observed (see Tables S1–S3 in the supplementary material). This high R$_s$ may obscure the accurate estimation of A and by extension E_{oo} in the temperature range of 260–300 K. Also, the data in Fig. 5(a) suggest that the $1/A$ values of the AIST sample may not be monotonous but exhibit a different slope at high temperatures. Hence, we did a fit to the AIST data with Eq. (9) for a restricted
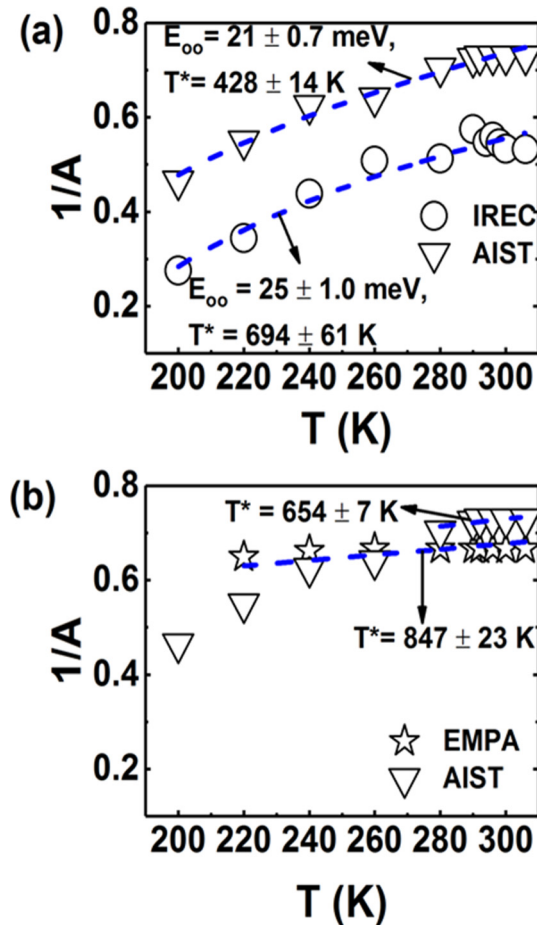
FIG. 5. Plot of $1/A$ vs T. The blue dashed lines represent fits in (a) to Eq. (9) (tunneling-enhanced rec. over defect distribution) and in (b) to Eq. (10) (recombination over defect distribution). The fit results for E_{oo} and T^* are given in the figures.

temperature range of 280–306 K and obtain $E_{oo} \sim 9$ meV, $T^* \sim 600$ K. Albeit the large data scattering, the same approach is employed for the IREC sample, yielding $E_{oo} \sim 10$ meV and $T^* \sim 2156$ K. These new E_{oo} values will still require a high doping of $\sim 5 \times 10^{17}$ cm^{-3} to be true.

For the EMPA sample, a fit of the $1/A$ data gives E_{oo} close to zero. This E_{00} suggests that tunneling for the EMPA sample is negligible in the temperature range of 200–300 K. Thus, the $1/A$ data of the EMPA sample were fit in Fig. 5(b) by Eq. (10) for SCR recombination via a defect distribution. This yielded $k_B T^* = 73$ meV and $A = 1.5$. With $T^* > T$ by a factor of ~ 3, a fit by the SCR defect distribution model appears justified. For the AIST sample, its moderate doping (10^{16}) even in the RLS state forward bias range [see Fig. 3(c)] of its doping profile excludes it from tunneling enhancement. We, therefore, tried a fit by Eq. (10) in the high temperature range and found $k_B T^* = 56$ meV, $A = 1.4$.

The corresponding fit to the IREC data is not displayed in Fig. 5(b) but was performed with the result $k_B T^* = 294 \pm 51$ meV.

3. Absorber bandgap

The bandgap energies at room temperature were obtained from the derivative of the EQE with respect to incident photon energy. Alternative values (given in parenthesis in Table II) were determined by a linear extrapolation of the EQE in the long wavelength regime to 0 nm (see Fig. S7 in the supplementary material). The later method is known to underestimate the real value of the bandgap;[51] however, we have used these lower bandgap values for SCAPS simulation and for our analytical model calculations to incorporate the effect of bandgap fluctuations[20,31] reported for kesterite solar cells. This will bring up higher current and lower voltage in simulation. The bandgap energies as determined from the derivative of EQE can be compared with the $E_{A,0}$ values of the samples as displayed in Table II. We see that $E_{A,0}$ is equal to the bandgap for the EMPA sample. It is greater than the bandgap for AIST, (by 0.2 eV) and IREC (by 0.3 eV) samples. Due to a slight temperature dependence of J_{oo}, a difference $E_{A,0} - E_{g,a}$ of around 0.075 eV is expected.[12]

E. Analytical models

Here, it shall be investigated how the red-light induced increase in $N_{A,a}$ would change the V_{oc} according to the models presented in Sec. I. Thereby, one has to regard the diode parameters A and E_A. First, we shall consider the SCR recombination model, with and without tunneling enhancement (TE-SCR), and then the non-inverted interface recombination model follows.

1. SCR recombination model

For this model, values of T^* as obtained in Fig. 5(b) were used, while E_{00} was varied according to its dependence on $N_{A,a}$ [see Eq. (8)]. Other relevant data for this test such as J_{sc} and $E_{g,a}$ were also adopted from the experimental results of the individual samples. Hence, in the following, it is tentatively postulated that $N_{A,a}$ has been determined correctly, but the experimental E_{oo} [which came out much larger than E_{oo} ($N_{A,a}$)] was not correctly determined. The question now is, based on E_{oo} ($N_{A,a}$), will tunneling enhanced recombination lead to rising or falling $V_{oc}(t)$ transients? Assuming a tunneling mass $m^* = 0.2 m_0$ (where m_0 denotes the electron mass, Ref. 44), the lifetimes $\tau_{n,a} = \tau_{p,a} = 2.5 \times 10^{-11}$ s for EMPA sample and $\tau_{n,a} = \tau_{p,a} = 3.5 \times 10^{-12}$ s for AIST sample[31,52] were estimated from a match of experimental V_{oc} values to V_{oc} values obtained by using Eq. (6). These lifetimes, coming out in the picosecond range,[52] are rather low. However, this is expected because the SCR model that we have used[33] for the calculation of these lifetimes does not include the correction factor for demarcation levels: the energetic range for effective recombination (Ref. 12, p. 46). It uses the complete defect distribution including those defects that are out of the demarcation levels and are not recombination active. As the complete defect density mathematically determines the lifetimes, they become very small. The real lifetimes responsible for SCR recombination in comparison to those presented here would be higher.

In the SCR recombination model, a metastable doping increase would reduce SCR recombination (see Fig. 7). Through algebraic manipulation of Eq. (6), at voltage $V = V_{oc}$, we calculated $V_{oc}(N_{A,a})$ numerically in two ways: By first excluding and second by including the tunneling contribution to the SCR recombination current. Figure 6 gives the calculated V_{oc} for both cases as a function of $N_{A,a}$ using the material and cell parameters of EMPA and AIST. It is seen that the model without tunneling gives increasing V_{oc} upon increasing $N_{A,a}$ for both samples. However, if the tunneling contribution is added to the space charge limited diode current, V_{oc} will decrease for a doping concentration exceeding 10^{17} cm^{-3}. This reversal of trend is due to the increasing electric field and a tunneling of charge carriers to the location of maximum recombination. Thus, the actual $V_{oc}(N_{A,a})$ relation and resulting $V_{oc}(t)$ will depend on the doping concentration and on E_{00}, as indicated in Table I and Fig. 7. Comparing V_{oc} at the estimated $N_{A,a}$ values of the relaxed state (7×10^{15} cm^{-3}) and the RLS state (8×10^{16} cm^{-3}) of the EMPA sample (see Table II), we see a V_{oc} increase of 46 mV for the case where $E_{00} = 0$, while for $E_{00} = E_{00}(N_{A,a})$, the V_{oc} increase is 18 mV. If we consider a higher $N_{A,a}$ (6×10^{17}) for the EMPA RLS state [extreme forward bias (0.5 V) region of its doping profile], we see straight away from Fig. 6 that for the TE-SCR model, $\Delta V_{oc}(N_{A,a}) = V_{oc}(N_{A,a\_RLS}) - (V_{oc}(N_{A,a\_Relaxed}))$ will be small, ∼7 mV. For the AIST sample, we estimate a V_{oc} increase of 30 mV for $E_{00} = 0$. Considering that the SCR recombination model does not incorporated factors such as potential fluctuations (Ref. 20) and the exact estimation of minority carrier lifetimes, the overall magnitude of V_{oc} calculated for a device using this model should be slightly higher than reality. Therefore, juxtaposing the results from the model with what we have obtained from $V_{oc}(t)$ experiment, the SCR model without tunneling is a good explanation for the $V_{oc}(t)$ observed for the EMPA and AIST samples.
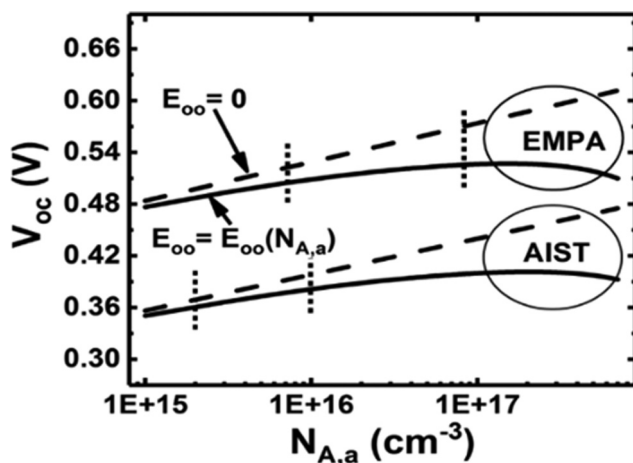

FIG. 6. Variation of open circuit voltage (V_{oc}) with the increase in absorber doping density ($N_{A,a}$) for the SCR recombination model with ($E_{00} = E_{00}(N_{A,a})$, solid line) and without ($E_{00} = 0$, dashed line) tunneling of the EMPA and AIST samples. The dotted vertical lines mark the experimental values of $N_{A,a}$ for the relaxed and RLS states.

2. Non-inverted IF recombination model

In order to test the applicability of the model of recombination at the interface between a non-inverted absorber and the buffer layer, we first tried to fit light JV curves of the three samples in SCAPS[53] with the condition that (1) the devices are limited by interface recombination and that (2) preferably their absorbers exhibit non-inverted interfaces. The formation of a non-inverted absorber interface requires a high p-type doping of the absorber, possibly in combination with negatively charged states (N_t^{IF}) at the absorber/buffer interface. The fitting parameters we obtained for each sample can be found in Tables S4–S6 in the supplementary material. While for the EMPA sample it was possible to realize a non-inverted absorber with only moderate interface state charge density (N_t^{IF}) due to its high RLS state doping, reasonable fitting of the light JV curves for IREC and AIST samples was not possible within a non-inverted absorber model because of their lower doping densities. Therefore, for the test of the non-inverted IF recombination model, we proceed with only the EMPA sample. From fitting of the EMPA sample light JV curve, specific parameters such as acceptor or donor defect capture cross sections ($\sigma_{d,a}$), density of acceptor defects at the absorber/buffer interface (N_t^{IF}), and $J_{sc}(N_{A,a})$ were obtained. These parameters are used as input in the analytical model equations in Sec. I B 2. Then, we varied the absorber doping in a range that encompasses the experimental values of the relaxed and the RLS states but (for study purposes) also extends beyond these. In addition, we allowed the interface charge (N_t^{IF}) to vary. The results in the form of calculated values of $E_{p,a}$, V_{oc}, A, and E_A are given in Tables VIII–XI of the Appendix. In a next step then, we carried out the same variation using SCAPS simulation. This allows us to assess our analytical model by comparison with simulated data.

By comparing SCAPS (Tables IV–VII) and calculated data from the analytical model (Tables VIII–XI), it can be seen that the non-inverted interface model can reproduce the trends for $E_{p,a}$, V_{oc}, A, and E_A simulated with SCAPS and gives absolute values within some reasonable error margin. Therefore, the formulas derived in this paper can be used to estimate the solar cell parameters of a device limited by interface recombination. This helps to assess whether recombination at a non-inverted interface is a possible model for a given device that is characterized by a rising $V_{oc}(t)$ trend and known doping concentration.

Coming back to the EMPA sample, it can now be asked whether the observed change of the solar cell parameters upon varying between relaxed and RLS state is in consistency with dominant recombination at the absorber/buffer interface. This can be done by the aid of Table III where the appropriate solar cell parameters from Tables IV–XI are collected. In particular, the calculated and simulated values of $E_{p,a}$, V_{oc}, A, and E_A for the cell in the RLS state ($N_{A,a} = 8 \times 10^{16}$ cm^{-3} and $N_t^{IF} = 4.8 \times 10^{10}$ cm^{-2}) and at the cell's relaxed state ($N_{A,a} = 7 \times 10^{15}$ cm^{-3} and $N_t^{IF} = 4.8 \times 10^{10}$ cm^{-2}) were collected, where available. For the RLS state again, the reasonable match between the model and simulation (in parenthesis) can be seen. As the relaxed state of the cell is located in the region of a symmetric absorber [Fermi energy ($E_{p,a}$) is approximately is in the middle of the interface bandgap, so it is neither inverted nor non-inverted], no analytical model data are
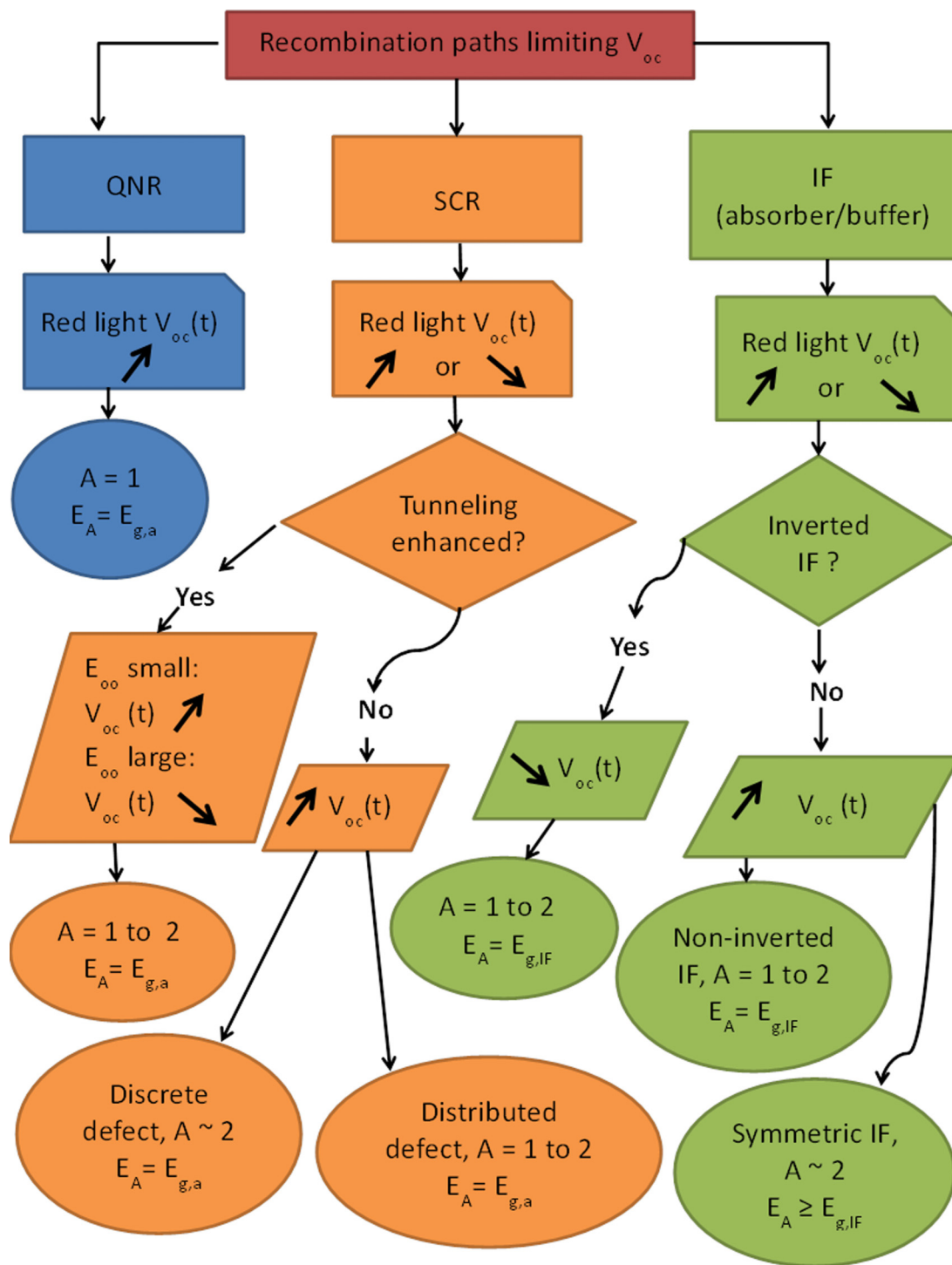
FIG. 7. Chart depicting the line of thought used for deciding which recombination process dominates at open circuit voltage. The direction of slope for the open circuit voltage transient $V_{oc}(t)$ (indicated by a rising or falling arrow) of a device exposed to red light after relaxation, in combination with its diode quality factor (A), activation energy of J_0 (E_A) and the magnitude of the characteristic tunneling energy (E_{oo}) are used as key determining factors for a decision on the dominant recombination path. For the creation of this flow chart, no Fermi level pinning was assumed.

TABLE III. Summary of the results from interface recombination IFR analytical model (and from SCAPS simulation) for the EMPA sample. For the symmetric absorber/buffer interface, the analytical model is not applicable (NA).

Absorber doping $N_{A,a}$ (cm^{-3})	Relaxed 7×10^{15}	RLS 8×10^{16}
Absorber/buffer interface	Symmetric	Non-inv.
$E_{p,a}^{IF}$ (eV)	0.59 (0.53)	0.26 (0.25)
A	NA (2.3)	1.2 (1.3)
E_A (eV)	NA (1.2)	1.0 (1.1)
V_{oc} (mV)	NA (340)	550 (520)
ΔV_{oc} (mV)	180	

available. The data in Table III can now be compared with the experimental ones in Table II. It is found that there are strong deviations in the diode factor, which according to the simulated values should change from 1.3 (RLS state) to 2.3 (relaxed state), while experimentally it is 1.3 (RLS state) to 1.5 (relaxed state). The ΔV_{oc} with respect to two states is also different. It is simulated to 180 mV while experimentally it is 32 mV. Therefore, judging from the magnitude of the V_{oc} increase and the change in A factor value, one can infer that IFR is not the dominant recombination mechanism for the EMPA sample studied in this work.

IV. DISCUSSION

A. Doping metastability

Both measurements of admittance spectroscopy and DLCP in this study have shown that upon red light exposure, the capacitance of the devices increases. This we assign to a doping metastability similar to what is known for Cu(In,Ga)Se$_2$ solar cells. Our finding is in principle agreement with results in Refs. 7, 14, and 16. An increase in C_{scr} is seen in the RLS state of the samples in Fig. 2 (compare dotted lines for both states of the samples; see also Table II for calculated values). In Figs. 3(a) and 3(c), we also see that the increase in $N_{A,a}$ is accompanied by a shrinkage of space charge width. Hence, from these results, we can say that the measured cells are indeed metastable upon exposure to red light. The doping increase is different for the investigated samples with the largest effect apparent in the EMPA and AIST samples where the calculated doping increases by one order of magnitude. From voltage-dependent admittance spectroscopy, we tried to determine whether interface states in the measured samples contribute to the admittance spectra,[28] and the results we obtained (see supplementary material Fig. S9) reveal that the activation energy of the defect states responsible for the main capacitance step is not voltage dependent. Thus, the admittance spectra cannot be interpreted as being influenced by IF defects. This result alone does not completely rule out the contribution of IF defects to the recombination current as interface defects will only contribute to an admittance spectrum if their energy states are intersected by the quasi-Fermi energy level during voltage variation. The activation energy of the main capacitance step, which is seen in the relaxed state admittance spectra, shifts to lower activation energies after RLS (see Fig. S8 in the supplementary material) for

the IREC and AIST samples. This would rule out the provenience of the admittance signature from a barrier at the back contact that should increase upon higher doping. Further evaluation to ascertain the presence or absence of a barrier is required.[16] For the EMPA sample, however, the relaxed state defect peak is still visible after RLS and the second more prominent peak can be attributed to the activation of an additional defect (see Fig. S8 in the supplementary material). Furthermore, for a bulk defect, there would be no change in activation energy except if a different deep defect is activated after RLS. Thus, an explanation for the red light effect on the activation energy for both voltage-dependent and zero bias admittance signatures would require further investigation.

B. Open circuit voltage metastability

In this work, it is initially postulated that the open circuit voltage transients $V_{oc}(t)$ measured originate from a metastable increase in doping concentration. This appears justified based on theoretical grounds where for most of the recombination mechanisms the relation between $N_{A,a}$ and V_{oc} is predicted. Nevertheless, one must state that the V_{oc} of a non-ideal solar cell also depends on the defect density. The open circuit voltage transients shown in Fig. 4 all have positive slopes ($dV_{oc}/dt > 0$). Thus, the device performance increases with the time of light exposure. Here, we have only tested red light effects. There may, however, be other light soaking effects by different light wavelengths. Reference 16 showed that doping increase can also be induced by white and blue light. This was interpreted as transmittance of blue light through the thin buffer to the absorber. In that respect, use of red light is less ambivalent as it is only absorbed in the kesterite layer. The positive slopes of $V_{oc}(t)$ that we obtain are similar to the results obtained for low gallium content Cu(In, Ga)Se$_2$ samples as reported in Refs. 7 and 10. They are dissimilar to the results of, e.g., high gallium content Cu(In,Ga)Se$_2$ devices, where a negative $V_{oc}(t)$ slope is an indication for interface recombination.[13] For the EMPA and AIST samples, the V_{oc} metastability goes along with an increase in capacitance, reduction in space charge width, and increased apparent doping concentration. In this paper, the combined increase in doping concentration and open circuit voltage is used to discuss the dominant recombination mechanism in the kesterite solar cells under investigation.

C. Region of dominant recombination

In Table I, different recombination mechanisms are listed which will yield positive $V_{oc}(t)$ slopes. These are the bulk recombination mechanisms in the QNR, in the SCR (with tunneling-enhanced SCR recombination being dependent on E_{00}), and at a non-inverted interface where the equilibrium Fermi level at the interface is closer to the valence band. Clearly, Table I excludes recombination at an inverted interface as the dominant mechanism for all three samples because this comes with a negative $V_{oc}(t)$ slope. In Table II, it is seen that the samples under investigation differ in several measured parameters such as diode quality factor, doping density, open circuit voltage, and relative activation energy. An overview of all these factors has been depicted by the way of a flow chart in Fig. 7. Therefore, we shall discuss the

dominant recombination mechanisms of the different samples independently.

1. EMPA sample

This device exhibits an activation energy approximately equal to its absorber bandgap. The A factor is weakly temperature dependent but could also be interpreted as being constant with a relaxed state value of 1.5 (the slightly smaller value in the RLS state could be interpreted as a measurement error). This A factor value being substantially larger than 1 rules out QNR recombination (see Fig. 7). By the way of the high doping concentration after RLS of 8×10^{16} cm^{-3}, the sample behavior could initially be explained by recombination at a non-inverted interface according to Table I. However, as explained in Sec. III E, a comparison with device simulation reveals strong contradictions to experiment in the quantities A factor and ΔV_{oc}. Therefore, a V_{oc} limitation by interface recombination for the EMPA sample must be ruled out.

According to Fig. 5(b), the temperature-dependent A factor of the EMPA sample would be in fair agreement with SCR recombination via a defect distribution with characteristic energy $k_B T^{\star}$ of 73 meV. From Fig. 6, we know that for SCR recombination via a defect distribution without tunneling, the expected V_{oc} increase amounts to about 46 meV. Considering a V_{oc} deficit due to potential fluctuations (not accounted for in this model but being possible[54,55] for this sample on account of its temperature dependent J_0[20] ($\alpha = 0.6 \pm 0.1$ meV K^{-1}) in the range of 280–300 K), and that the defect density used for calculations in the SCR model may be overestimated, this result is not too far from the experimentally observed V_{oc} increase of 32 mV. Also, the activation energy $E_{A,0}$ of 1.1 eV is not in contradiction to SCR recombination via a defect distribution. Thus, we conclude that the EMPA sample is limited by recombination in the SCR via an exponential defect distribution.

2. AIST sample

This device exhibits an A factor of 1.4 at room temperature which is closer to the prediction for QNR recombination ($A = 1$). However, at lower temperatures, the A factor becomes temperature dependent which is no longer consistent with QNR recombination but an indication of recombination via a defect distribution in the SCR with or without tunneling involvement. The non-inverted interface model was ruled out for this sample because a simulated device could not be fitted accordingly. Also this sample has an A factor approximately the same in the relaxed and RLS states (see Table II) which is also in contradiction to interface recombination as a change in doping (see 1×10^{16} to 2×10^{15} cm^{-3} in Table VI) would induce a change in the A factor for this model. Furthermore, the non-inverted interface model would require a V_{oc} increase of over 100 mV (Table V) if transiting from the relaxed to the RLS state, in contradiction to our experimental findings.

Different scenarios of SCR recombination have been tested for the AIST sample. From the fit of the $1/A$ values in Fig. 5(a) using the complete temperature range (200–300 K), we found a tunneling energy of 21 meV. This relatively high value requires a doping concentration $N_{A,a}$ above 10^{18} cm^{-3}. Such a large $N_{A,a}$ value exceeds both the minimum and forward bias doping concentration in the

DLCP plot by two orders of magnitude. Furthermore, the evaluation of the $J_o(T)$ data in the complete temperature range gives a J_{oo} value of around 1 mA cm^{-2}. This is inconsistent with $J_{oo} = 10^8 - 10^9$ mA cm^{-2} as calculated using standard material parameters for the AIST sample, assuming SCR recombination.[20] In addition, the temperature coefficient of the activation energy $\alpha = 3.1 \pm 0.3$ meV K^{-1} comes out very large when fitting the complete temperature range. Therefore, it is assumed that given the increase in series resistance R_s toward lower temperature, such a large R_s is not fully compensated in the plots of Fig. S4 in the supplementary material and mimic a too large A factor. In order to test this hypothesis, only the temperature range of 280–306 K as a limited extreme was evaluated. For this temperature range, the reference current density comes out as $J_{oo} = 10^9$ mA cm^{-2}, and the temperature coefficient of the activation energy comes out as $\alpha = 0.5$ meV K^{-1}. Now, assuming tunneling-enhanced SCR recombination via an exponential defect distribution, we demonstrate in Sec. III E that this sample has a doping that is too low to allow for substantial TE-SCR recombination. Assuming the SCR recombination model without tunneling to dominate around room temperature, we found that it would yield a V_{oc} increase from relaxed to the RLS state of 27 mV. This increase, as the result of the measured $N_{A,a}$ increase, is in close agreement with the V_{oc} increase of 24 mV experimentally measured for this sample. Thus, the dominant recombination mechanism for the AIST sample is allocated to SCR recombination (without tunneling enhancement) over a defect distribution.

3. IREC sample

This sample is considered in close similarity to the AIST sample, however with larger (decaying deeper into the bandgap) characteristic tail state energy of 294 ± 51 meV in the temperature range of 280–306 K. Thus, also for this sample, recombination in the SCR over a defect distribution without tunneling contribution is assumed. Note that the R_s increase toward low temperature is even more severe for this sample in comparison to the AIST sample. There, however, remains to be discussed the very large V_{oc} increase with time given the small doping increase of the IREC sample. We attribute this large increase to a combination of metastable doping increase upon exposure to red light and the effect of an anomaly activated by sample relaxation. A close examination of the start point of the $V_{oc}(t)$ range measured for this sample (49–101 mV) in comparison to AIST (364–388 mV) and EMPA (470–502 mV) points to this. Hence, in the unique case of the IREC sample, the increased doping (which we confirm with DLCP and admittance spectroscopy) may not be completely responsible for the large ΔV_{oc} seen. Further investigation is required for a better understanding of this anomaly.

V. CONCLUSION

We have used admittance spectroscopy and capacitance voltage profiling techniques to establish that there is a doping metastability in kesterite absorber layers after exposure to red light. The doping density in kesterite layers from different preparation methods increases after red light exposure and causes an increase in the space charge capacitance and a shrinking of the space charge

width. This information has been used to interpret the observed open circuit voltage increase during red light soaking for the AIST and EMPA samples. In order to test a different recombination mechanism, in this case, a non-inverted interface device limited by interface recombination via discrete defects and analytical expressions for the activation energy of the saturation current density (E_A), for the diode quality factor (A), and for the dependency $V_{oc}(N_{A,a})$, have been derived. By comparison between modeled data and simulated data, a reasonable match is found, revealing the applicability of the model for recombination at a non-inverted absorber interface. By a comparison of theory and experiment, it is found that the kesterite solar cells under investigation are not limited by recombination at the interface, neither at a possibly inverted interface nor at a possibly non-inverted one. Instead, the devices are limited by bulk recombination, where space charge region recombination over tail states (without tunneling enhancement) is the most plausible explanation. These results help answer the long-lasting debate on the origin of the V_{oc} limitation of low bandgap kesterite devices that appear not to be located at its heterojunction interface.

SUPPLEMENTARY MATERIAL

See the supplementary material for additional information regarding the J–V analysis, EQE, admittance spectroscopy, SCAPS simulation parameters, and the analytical model for interface recombination.

ACKNOWLEDGMENTS

This work was supported by the German Academic Exchange Service (DAAD), Tertiary Education Trust Fund (Tetfund) Nigeria, and partly by the European Union H2020 project “STARCELL”; their support is hereby gratefully acknowledged. The authors also want to thank T. Hoelscher for insightful discussions and laboratory assistance.

APPENDIX: SOLAR CELL PARAMETERS FROM IFR MODEL AND RELATED FIGURES

1. Simulated solar cell parameters

Tables IV–VII show the SCAPS-determined influence of $N_{A,a}$ and N_t^{IF} on cell parameters $E_{p,a}$, V_{oc}, A, and E_A of a device limited by interface recombination. Starting with Table IV, the hole Fermi energy at the interface ($E_{p,a}^{IF}$) is the largest in the upper left corner of the table (cell printed in blue format). This marks the position of the lowest absorber doping and lowest negative interface charge, giving rise to an inversion of the p-type absorber layer (for definition of $E_{p,a}^{IF}$, see Fig. 1). From there, increasing both $N_{A,a}$ and N_t^{IF} reduces $E_{p,a}$ up to the minimum in the lower right corner (cell printed in red format) where the absorber obviously is non-inverted. Between these extremes, we find combinations of $N_{A,a}$ and N_t^{IF} where the absorber interface is what is called symmetric, i.e., where the Fermi energy approximately equals the value of midgap energy, $E_g/2$. A look at the A factor from SCAPS simulation in Table II helps define this symmetric region even better. The A factor values were obtained by fitting the dark JV curves of the simulated device for the different combinations of $N_{A,a}$ and N_t^{IF} given in the table. It is found that the A factor along an imagined line (follow dotted arrow in the table) from the upper left to the lower right corner, i.e., from the most inverted to the most non-inverted absorber, approaches 1 in the corners and passes a maximum of approximately 2 in the middle region.[12] Now, the combinations of $N_{A,a}$ and N_t^{IF} where the A factor exceeds 1.5 are considered as the “symmetric region.” All parameters in this “symmetric region” are printed in shaded format. In Table IV, it is seen that this region has $E_{p,a}$ indeed close to midgap. Approximately, this is also the region where E_A, the activation energy of J_0, slightly exceeds 1.1 (with the borderline column of $N_{A,a} = 4 \times 10^{16}$ cm^{-2}). The symmetric absorber also bears low V_{oc} values.

2. Solar cell parameters from analytical models

In Tables VIII–XI, the same set of parameters as in Tables IV–VII are given. Here, $E_{p,a}$, V_{oc}, A, and E_A are calculated data. Using the classification from these tables, the non-inverted IF model, as formulated in Eqs. (13), (19), (16), and (17) was used for high $N_{A,a}$ and N_t^{IF}, while data for the inverted absorber IF were calculated from the formulas in Ref. 29 for low $N_{A,a}$ and N_t^{IF}.

3. Figures for recombination paths limiting open circuit voltage (V_{oc})

From Fig. 7, one can discriminate between three Shockley–Read–Hall recombination paths that can limit the open circuit voltage of a device. We note here that the direction of slope for the open circuit voltage transients $V_{oc}(t)$ as depicted here is applicable

TABLE IV. SCAPS simulated barrier height for holes ($E_{p,a}$) at equilibrium (EMPA parameters as in Table S4 in the supplementary material except for varied $N_{A,a}$ and N_t^{IF}). Region with entries shaded gray represents the symmetric region. Bold formatted cell marks the highest $E_{p,a}$ value, while italic formatted cell marks the lowest $E_{p,a}$ value.

	$N_{A,a} \times 10^{15}$ (cm^{-3})									
	1	2	3	4	6	8	10	40	80	100
$N_t^{IF} \times 10^{10}$ cm^{-2}	$E_{p,a}$ (meV) inverted IF							$E_{p,a}$ (meV) non-inverted IF		
3	**727**	685	653	627	586	554	527	346	263	239
4	711	669	637	612	571	540	514	337	260	233
4.8	698	656	620	599	559	528	503	330	251	229
7.8	647	607	577	553	515	486	462	304	234	213
10	609	570	542	519	483	455	433	286	221	*203*

Published under an exclusive license by AIP Publishing

TABLE V. SCAPS simulated open circuit voltage (V_{oc}) (EMPA parameters as in Table S4 in the supplementary material except for varied $N_{A,a}$ and N_t^{IF}). Region with entries shaded gray represents the symmetric region.

$N_t^{IF} \times 10^{10}$ cm^{-2}	$N_{A,a} \times 10^{15}$ (cm^{-3})									
	1	2	3	4	6	8	10	40	80	100
	V_{oc} (meV) inverted IF							V_{oc} (meV) non-inverted IF		
3	435	400	373	351	312	289	323	471	510	520
4	420	385	358	335	297	314	349	478	514	523
4.8	408	372	345	322	293	336	367	484	517	536
7.8	361	324	300	332	380	407	425	500	526	533
10	325	335	375	400	428	444	455	510	531	538

TABLE VI. SCAPS simulated diode quality factor (A). Non-inverted IF model on the right hand side of green border, inverted IF model on the LHS of the table (low $N_{A,a}$). Region with entries shaded gray represents the symmetric region. The dotted arrow shows the movement from the most inverted point of the absorber to the most non-inverted point.

$N_t^{IF} \times 10^{10}$ cm^{-2}	$N_{A,a} \times 10^{15}$ (cm^{-3})									
	1	2	3	4	6	8	10	40	80	100
	A (SCAPS) inverted IF							A (SCAPS) non-inverted IF		
3	1.3	1.4	1.4	1.5	1.5	2.3	2.3	1.5	1.3	1.2
4	1.3	1.4	1.4	1.5	1.6	2.0	2.3	1.4	1.3	1.2
4.8	1.3	1.4	1.5	1.5	1.9	2.2	2.1	1.4	1.3	1.2
7.8	1.3	1.4	2.3	2.0	2.2	1.9	1.9	1.4	1.2	1.2
10	1.3	2.0	2.2	2.0	1.9	1.8	1.7	1.3	1.2	1.2

TABLE VII. SCAPS simulated activation energy E_A of Jo (EMPA parameters as in Table S4 in the supplementary material except for varied $N_{A,a}$ and N_t^{IF}). Region with entries shaded gray represents the symmetric region.

$N_t^{IF} \times 10^{10}$ cm^{-2}	$N_{A,a} \times 10^{15}$ (cm^{-3})									
	1	2	3	4	6	8	10	40	80	100
	E_A (SCAPS) inverted IF							E_A (SCAPS) non-inverted IF		
3	1.1	1.1	1.0	1.0	1.0	1.2	1.2	1.2	1.1	1.1
4	1.0	1.0	1.0	1.0	1.0	1.3	1.2	1.2	1.1	1.1
4.8	1.0	1.0	1.0	1.0	1.2	1.2	1.2	1.2	1.1	1.1
7.8	1.0	1.0	1.1	1.3	1.3	1.2	1.2	1.2	1.1	1.1
10	1.0	1.5	1.4	1.3	1.2	1.2	1.2	1.2	1.1	1.1

TABLE VIII. Calculated barrier height for holes ($E_{p,a}$) from Eq. (14) under equilibrium conditions at the absorber–buffer interface (EMPA parameters as in Table S4 in the supplementary material except for varied $N_{A,a}$ and N_t^{IF}).

$N_t^{IF} \times 10^{10}$ cm^{-2}	$N_{A,a} \times 10^{15}$ (cm^{-3})									
	1	2	3	4	6	8	10	40	80	100
	$E_{p,a}$ (meV) inverted IF							$E_{p,a}$ (meV) non-inverted IF		
3	829	773	733	701	651			370	271	243
4	810	754	715	684				360	265	237
4.8	794	740	701	670				352	259	232
7.8	737	685						324	239	215
10	692							305	226	203

TABLE IX. Calculated open circuit voltage (V_{oc}) according to the non-inverted IF model (to the right of table) from Eq. (20) and according to the inverted IF model (to the left of table) from Eq. (17) in Ref. 29 (EMPA parameters as in Table S4 in the supplementary material except for varied $N_{A,a}$ and N_t^{IF}).

$N_t^{IF} \times 10^{10}$ cm^{-2}	$N_{A,a} \times 10^{15}$ (cm^{-3})									
	1	2	3	4	6	8	10	40	80	100
	V_{oc} (mV) inverted IF							V_{oc} (mV) non-inverted IF		
3	413	369	337	305	261			495	544	556
4	391	347	313	284				504	548	559
4.8	374	330	296	270				510	551	561
7.8	309	269						530	561	569
10	265							541	567	574

TABLE X. Calculated diode quality factor (A) according to the non-inverted IF model (to the right of table) from Eq. (17) and according to the inverted IF model (to the left of table) from Eq. (13) in Ref. 29 (EMPA parameters as in Table S4 in the supplementary material except for varied $N_{A,a}$ and N_t^{IF}).

$N_t^{IF} \times 10^{10}$ cm^{-2}	$N_{A,a} \times 10^{15}$ (cm^{-3})									
	1	2	3	4	6	8	10	40	80	100
	A inverted IF							A non-inverted IF		
3	1.2	1.3	1.3	1.4	1.4			1.4	1.2	1.2
4	1.2	1.3	1.3	1.4				1.4	1.2	1.2
4.8	1.2	1.3	1.3	1.4				1.4	1.2	1.1
7.8	1.2	1.3						1.3	1.1	1.1
10	1.2							1.2	1.1	1.1

TABLE XI. Calculated activation energy E_A of J_o according to the non-inverted IF model (to the right of table) from Eq. (18) and according to the inverted IF model (to the left of table) from Eq. (14) in Ref. 29 (EMPA parameters as in Table S4 in the supplementary material except for varied $N_{A,a}$ and N_t^{IF}).

$N_t^{IF} \times 10^{10}$ cm^{-2}	$N_{A,a} \times 10^{15}$ (cm^{-3})									
	1	2	3	4	6	8	10	40	80	100
	E_A (eV) inverted IF							E_A (eV) non-inverted IF		
3	1.2	1.2	1.2	1.2	1.2			1.0	1.0	1.0
4	1.2	1.2	1.2	1.2				1.0	1.0	1.0
4.8	1.2	1.2	1.2	1.2				1.0	1.0	1.0
7.8	1.3	1.3						1.0	1.0	1.0
10	1.4							1.0	1.0	1.0

only to a device that is exposed to red light after undergoing relaxation. Exposure to light of different wavelengths (blue or white light, for instance) may give different results. We see in this figure that the decision path for QNR recombination as the dominant recombination path is straightforward. A rising $V_{oc}(t)$ is expected with the A factor being equal to 1 and $E_A = E_{g,a}$. The path to decide on SCR recombination is, however, not straightforward. $V_{oc}(t)$ can rise or fall depending on whether tunneling enhancement is involved. Note that, to obtain a falling $V_{oc}(t)$ due to the effect of tunneling enhanced recombination in the SCR, the doping density of such a device must be high ($\geq 10^{17}$ cm^{-3}). Furthermore, the A factor for

SCR recombination can vary between 1 and 2, depending on whether the defects in the bandgap are discrete or exponentially distributed. The addition of tunneling enhancement to the recombination process can also cause the A factor to vary between 1 and 2. The activation energy of J_o E_A should equal $E_{g,a}$. For a decision on interface recombination also, we see that $V_{oc}(t)$ can rise or fall. In this case, however, the difference in the slope of $V_{oc}(t)$ is dependent on the devices' absorber–buffer interface. If the absorber is inverted, $V_{oc}(t)$ will fall, and if it is symmetric (based on SCAPS simulation) or non-inverted, $V_{oc}(t)$ will rise. The A factor ranges between 1 and 2 for a non-inverted interface;
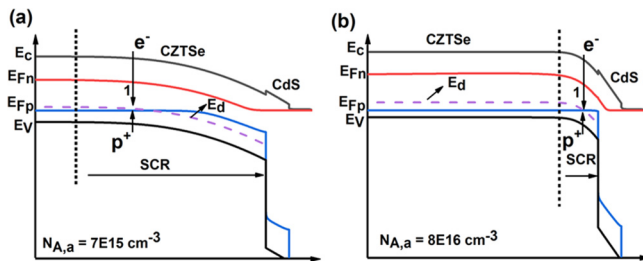
FIG. 8. Schematic band diagram illustrating the effect of increased doping ($N_{A,a}$) on space charge region recombination (SCR) in CZTSe absorber. (a) Low $N_{A,a}$ allows a wide space charge region. 1 marks a SCR defect recombination site. (b) In comparison, high $N_{A,a}$ narrows the SCR width and increases band bending in the CdS layer. It also makes the exponential decay of the carrier concentrations n and p steeper.[58] Hence, the position n = p of maximum recombination is shifted to a smaller range with SCR narrowing. This leads to a reduced zone of effective recombination; leading to a V_{oc} increase with $N_{A,a}$ increase.

it is ∼2 for a symmetric IF. E_A, however, can be less than or greater than $E_{g,a}$ ($E_A \neq E_{g,a}$) because E_A is equal to the bandgap at the IF (Fig. 1).

In Fig. 8, the impact of increased absorber doping on the SCR width (W_a) and by extension SCR recombination is depicted. Increased absorber doping is accompanied by an increase of the electric field strength (F_m) at the point of maximum carrier recombination n = p. Therefore a plot of the carrier concentrations within the SCR with respect to distance from the pn junction for Fig. 8(b) would exhibit a steeper decline (n-away and p-towards the pn junction) in comparison to Fig. 8(b). This implies that there would be less carriers available for recombination at the position n = p in Fig. 8(b) leading to a reduced zone of maximum recombination for SCR recombination. This is accompanied by a V_{oc} increase.

DATA AVAILABILITY

The data that support the findings of this study are available from the corresponding author upon reasonable request.

REFERENCES

[1]S. Giraldo, Z. Jehl, M. Placidi, V. Izquierdo-Roca, A. Pérez-Rodríguez, and E. Saucedo, Adv. Mater. **31**, 1806692 (2019).
[2]U. Rau, M. Schmitt, J. Parisi, W. Riedl, and F. Karg, Appl. Phys. Lett. **73**, 223 (1998).
[3]T. Meyer, M. Schmidt, F. Engelhardt, J. Parisi, and U. Rau, Eur. Phys. J.: Appl. Phys. **8**, 43 (1999).
[4]S. Lany and A. Zunger, J. Appl. Phys. **100**, 113725 (2006).
[5]M. Maciaszek and P. Zabierowski, J. Appl. Phys. **119**, 215103 (2016).
[6]T. Eisenbarth, R. Caballero, M. Nichterwitz, C. A. Kaufmann, H. W. Schock, and T. Unold, J. Appl. Phys. **110**, 094506 (2011).
[7]F. Engelhardt, M. Schmidt, T. Meyer, O. Seifert, J. Parisi, and U. Rau, Phys. Lett. A **245**, 489 (1998).
[8]M. Igalson and H. W. Schock, J. Appl. Phys. **80**, 5765 (1996).
[9]J. T. Heath, J. D. Cohen, and W. N. Shafarman, Thin Solid Films **431**, 426 (2003).
[10]F. Obereigner, N. Barreau, W. Witte, and R. Scheer, J. Appl. Phys. **117**, 055704 (2015).

[11]M. N. Ruberto and A. Rothwarf, J. Appl. Phys. **61**, 4662 (1987).
[12]R. Scheer and H.-W. Schock, *Chalcogenide Photovoltaics—Physics, Technologies and Thin Film Devices* (Wiley-VCH, Weinheim, 2011).
[13]S. Zahedi-Azad and R. Scheer, Phys. Status Solidi C **14**, 1600203 (2017).
[14]M. A. Lloyd, B. E. McCandless, and R. Birkmire, "Analysis of high-Voc single-crystal CZTSe solar cells via admittance spectroscopy," in *2018 IEEE 7th World Conference on Photovoltaic Energy Conversion (WCPEC) (A Joint Conference of 45th IEEE PVSC, 28th PVSEC & 34th EU PVSEC)* (IEEE, 2018), p. 2507.
[15]M. J. Koeper, C. J. Hages, J. V. Li, D. Levi, and R. Agrawal, Appl. Phys. Lett. **111**, 142105 (2017).
[16]V. Kosyak, N. Ross, and C. Platzer-Björkman, J. Phys. D: Appl. Phys. **53**, 185108 (2020).
[17]M. A. Lloyd, A. G. Kuba, B. E. McCandless, and R. Birkmire, J. Appl. Phys. **128**, 143102 (2020).
[18]M. J. Koeper, C. J. Hages, J. V. Li, D. Levi, and R. Agrawal, "Admittance spectroscopy in CZTSSe: Metastability behavior and voltage dependent defect study," in *2016 IEEE 43rd Photovoltaic Specialists Conference (PVSC)* (IEEE, 2016), p. 2200.
[19]L. Grenet, P. Grondin, K. Coumert, N. Karst, F. Emieux, F. Roux, R. Fillon, G. Altamura, H. Fournier, P. Faucherand, and S. Perraud, Thin Solid Films **564**, 375 (2014).
[20]C. J. Hages, N. J. Carter, R. Agrawal, and T. Unold, J. Appl. Phys. **115**, 234504 (2014).
[21]H. Yin, A. Akey, and R. Jaramillo, Phys. Rev. Mater. **2**, 084602 (2018).
[22]Z. K. Yuan, S. Y. Chen, H. J. Xiang, X. G. Gong, A. Walsh, J. S. Park, I. Repins, and S. H. Wei, Adv. Funct. Mater. **25**, 6733 (2015).
[23]Y. F. Qi, D. X. Kou, W. H. Zhou, Z. J. Zhou, Q. W. Tian, Y. N. Meng, X. S. Liu, Z. L. Du, and S. X. Wu, Energy Environ. Sci. **10**, 2401 (2017).
[24]H. Tampo, S. Kim, T. Nagai, H. Shibata, and S. Niki, ACS Appl. Mater. Interfaces **11**, 13319 (2019).
[25]L. Grenet, M. A. A. Suzon, F. Emieux, and F. Roux, ACS Appl. Energy Mater. **1**, 2103 (2018).
[26]A. Polizzotti, I. L. Repins, R. Noufi, S. H. Wei, and D. B. Mitzi, Energy Environ. Sci. **6**, 3171 (2013).
[27]I. L. Repins, M. J. Romero, J. V. Li, S.-H. Wei, D. Kuciauskas, C.-S. Jiang, C. Beall, C. DeHart, J. Mann, and W.-C. Hsu, IEEE J. Photovolt. **3**, 439 (2012).
[28]T. Hoelscher, T. Schneider, M. Maiberg, and R. Scheer, Prog. Photovoltaics **26**, 934 (2018).
[29]H. Wilhelm, H. W. Schock, and R. Scheer, J. Appl. Phys. **109**, 084514 (2011).
[30]V. Nadenau, U. Rau, A. Jasenek, and H. W. Schock, J. Appl. Phys. **87**, 584 (2000).
[31]M. Grossberg, J. Krustok, C. J. Hages, D. M. Bishop, O. Gunawan, R. Scheer, S. M. Lyam, H. Hempel, S. Levcenco, and T. Unold, J. Phys.: Energy **1**, 044002 (2019).
[32]U. Rau, A. Jasenek, H. W. Schock, F. Engelhardt, and T. Meyer, Thin Solid Films **361**, 298 (2000).
[33]U. Rau, Appl. Phys. Lett. **74**, 111 (1999).
[34]F. Padovani and R. Stratton, Solid-State Electron. **9**, 695 (1966).
[35]G. Hurkx, D. Klaassen, and M. Knuvers, IEEE Trans. Electron Devices **39**, 331 (1992).
[36]S. G. Haass, C. Andres, R. Figi, C. Schreiner, M. Burki, Y. E. Romanyuk, and A. N. Tiwari, Adv. Energy Mater. **8**, 1701760 (2018).
[37]A. Hernández-Martínez, M. Placidi, L. Arqués, S. Giraldo, Y. Sánchez, V. Izquierdo-Roca, P. Pistor, M. Valentini, C. Malerba, and E. Saucedo, ACS Appl. Energy Mater. **1**, 1981 (2018).
[38]J. T. Heath, J. D. Cohen, and W. N. Shafarman, J. Appl. Phys. **95**, 1000 (2004).
[39]H. Kempa, T. Rissom, U. Hlawatsch, M. Gaudig, F. Obereigner, C. A. Kaufmann, and R. Scheer, Thin Solid Films **535**, 340 (2013).
[40]F. Obereigner and R. Scheer, EPJ Photovoltaics **5**, 50101 (2014).
[41]O. Gunawan, T. Gokmen, C. W. Warren, J. D. Cohen, T. K. Todorov, D. A. R. Barkhouse, S. Bag, J. Tang, B. Shin, and D. B. J. A. P. L. Mitzi, Appl. Phys. Lett. **100**, 253905 (2012).

[42] G. Larramona, S. Levcenko, S. Bourdais, A. Jacob, C. Chone, B. Delatouche, C. Moisan, J. Just, T. Unold, and G. Dennler, Adv. Energy Mater. **5**, 1501404 (2015).

[43] S. Levcenko, J. Just, A. Redinger, G. Larramona, S. Bourdais, G. Dennler, A. Jacob, and T. Unold, Phys. Rev. Appl. **5**, 024004 (2016).

[44] C. Persson, J. Appl. Phys. **107**, 053710 (2010).

[45] T. P. Weiss, S. Nishiwaki, B. Bissig, S. Buecheler, and A. N. Tiwari, Phys. Chem. Chem. Phys. **19**, 30410 (2017).

[46] D. Mergel and Z. Qiao, J. Appl. Phys. **95**, 5608 (2004).

[47] J. V. Li and G. Ferrari, *Capacitance Spectroscopy of Semiconductors* (Pan Stanford, 2018).

[48] D. Abou-Ras, T. Kirchartz, and U. Rau, *Advanced Characterization Techniques for Thin Film Solar Cells* (Wiley Online Library, 2011).

[49] U. Rau and H.-W. Schock, Appl. Phys. A **69**, 131 (1999).

[50] S. S. Hegedus and W. N. Shafarman, Prog. Photovoltaics **12**, 155 (2004).

[51] R. Carron, C. Andres, E. Avancini, T. Feurer, S. Nishiwaki, S. Pisoni, F. Fu, M. Lingg, Y. E. Romanyuk, and S. Buecheler, Thin Solid Films **669**, 482 (2019).

[52] C. J. Hages, A. Redinger, S. Levcenko, H. Hempel, M. J. Koeper, R. Agrawal, D. Greiner, C. A. Kaufmann, and T. Unold, Adv. Energy Mater. **7**, 1700167 (2017).

[53] M. Burgelman, P. Nollet, and S. Degrave, Thin Solid Films **361**, 527 (2000).

[54] M. Lang, C. Zimmermann, C. Krämmer, T. Renz, C. Huber, H. Kalt, and M. Hetterich, Phys. Rev. B **95**, 155202 (2017).

[55] M. Yakushev, J. Márquez-Prieto, I. Forbes, P. Edwards, V. Zhivulko, A. Mudryi, J. Krustok, and R. Martin, J. Phys. D: Appl. Phys. **48**, 475109 (2015).

[56] C. T. Sah, R. N. Noyce, and W. Shockley, "Carrier generation and recombination in pn junctions and pn junction characteristics," Proc. IRE **45**(9), 1228–1243 (1957).